1 **The D614G Mutation Enhances the Lysosomal Trafficking of SARS-CoV-2 Spike**

2

3 *Chenxu Guo, *Shang-Jui Tsai, *Yiwei Ai, #Maggie Li, #Andrew Pekosz, @Andrea Cox,

4 ^Nadia Atai, and *Stephen J. Gould

5

6 *Department of Biological Chemistry, Johns Hopkins University, School of Medicine,

7 725 North Wolfe Street, Baltimore, MD, 21205

8

9 #Department of Microbiology and Immunology, Johns Hopkins University, School of

10 Public Health, 615 North Wolfe Street, Baltimore, MD 21205

11

12 @Department of Medicine, Department of Microbiology and Immunology, Johns Hopkins

13 University, School of Medicine, 725 North Wolfe Street, Baltimore, MD, 21205

14

15 ^Capricor, Inc. 8840 Wilshire Blvd, Beverly Hills, CA 90211

16

17

18

19

20

21

22   Correspondence:

23   Name: Stephen J. Gould Ph.D

24   Address: 725 North Wolfe Street, Baltimore, MD 21205

25   Phone number: 443 847 9918

26   Email: sgould@jhmi.edu

27

28

29   Running title: Lysosomal sorting of D614G spike

30

31   Key Words: COVID19, SARS-CoV-2, spike, lysosomes, protein sorting, Golgi,

32   coronavirus, infection

33

34 **Abstract**

35 The spike D614G mutation increases SARS-CoV-2 infectivity, viral load, and transmission

36 but the molecular mechanism underlying these effects remains unclear. We report here

37 that spike is trafficked to lysosomes and that the D614G mutation enhances the lysosomal

38 sorting of spike and the lysosomal accumulation of spike-positive punctae in SARS-CoV-

39 2-infected cells. Spike trafficking to lysosomes is an endocytosis-independent, V-

40 ATPase-dependent process, and spike-containing lysosomes drive lysosome clustering

41 but display poor lysotracker labeling and reduced uptake of endocytosed materials. These

42 results are consistent with a lysosomal pathway of coronavirus biogenesis and raise the

43 possibility that a common mechanism may underly the D614G mutation's effects on spike

44 protein trafficking in infected cells and the accelerated entry of SARS-CoV-2 into

45 uninfected cells.

Introduction

46

47 COVID-19 (coronavirus infectious disease 2019) is caused by infection with the

48 enveloped virus SARS-CoV-2, a member of the betacoronavirus family (Coronaviridae

49 Study Group of the International Committee on Taxonomy of, 2020; Zhou et al., 2020). In

50 just one year, SARS-CoV-2 has infected >65 million people, killed >1.5 million people,

51 and caused extensive morbidity among survivors. Of all the RNA viruses, coronavirus

52 have the largest genomes, encoding more than two dozen proteins (Wang et al., 2020).

53 However, leading vaccine candidates elicit immunity to just a single protein, spike (Poland

54 et al., 2020), which mediates the first two steps in the replication cycle: cell binding and

55 fusion of viral and cellular membranes.

56

57 SARS-CoV-2 entry leads to translation of its viral genomic RNA (gRNA) into the orf1a

58 and orf1a/b polyproteins (V'Kovski et al., 2020). These are then processed to generate

59 16 non-structural proteins (nsps) that reprogram the cell for viral replication and drive the

60 synthesis of subgenomic viral mRNAs. These encode the four major structural proteins

61 of mature virions (nucleocapsid (N), spike (S), membrane (M), and envelope (E)) and nine

62 additional ORFs (3a, 3b, 6, 7a, 7b, 8, 9b, 9c, & 10) that together drive virus particle

63 assembly and release. The spike, membrane and envelope proteins are sufficient to drive

64 the formation of virus-like-particles and are thought to drive virion budding as well. This

65 occurs following the synthesis of these proteins in the endoplasmic reticulum (ER) and

66 their vesicle-mediated transport to the ER-Golgi intermediate compartment (ERGIC)

67 (Ruch and Machamer, 2012; Ujike and Taguchi, 2015). As for how fully-formed virus

68 particles (Yao et al., 2020) are released from infected cells, the prevailing model has been

4

69   that they are released by the biosynthetic secretory pathway (Ujike and Taguchi, 2015).

70   However, Altan-Bonnet and colleagues recently demonstrated that egress of mouse

71   hepatitis virus (MHV, another betacoronavirus) does not require the biosynthetic

72   secretory pathway, and instead uses an Arl8-dependent, lysosomal pathway of egress

73   (Ghosh et al., 2020).

74

75   Shortly after its entry into the human population, a variant strain of SARS-CoV-2 arose

76   that displays multiple hallmarks of increased viral fitness, including a higher rate of

77   transmission, elevated viral load *in vivo*, and enhanced infectivity *in vitro* (Hou et al., 2020;

78   Korber et al., 2020; Lorenzo-Redondo et al., 2020) This variant contains a mutation in the

79   spike gene, D614G, that replaces the aspartate at position 614 with a glycine. This

80   mutation lies N-terminal to the polybasic site cleavage site (682RRAR685), a cleavage

81   event that is essential to virus replication and generates the non-covalently associated N-

82   terminal S1 and C-terminal S2 proteins (Hoffmann et al., 2020a; Hoffmann et al., 2020b).

83   The spike S1 domain binds SARS-CoV-2 receptors, primarily angiotensin converting

84   enzyme-2 (ACE2) (Hoffmann et al., 2020b; Matheson and Lehner, 2020; Zhou et al.,

85   2020)(Wrapp et al., 2020) but also neuropilin-1 (Cantuti-Castelvetri et al., 2020; Daly et

86   al., 2020), and yet, there is as yet no evidence that the D614G mutation alters the affinity

87   of S1 for its receptors or for target cells. In fact, ultrastructural and biochemical analyses

88   of matched D614 and G614 SARS-CoV-2 viruses show no differences in their

89   appearance in electron micrographs, and also no difference in levels of virion-associated

90   spike proteins (Hou et al., 2020).

91

92 Here we extend our understanding of the spike D614G mutation by demonstrating that it

93 shifts spike protein trafficking towards the lysosome and away from organelles of the

94 biosynthetic secretory pathway. This shift is reflected in the localization of SARS-CoV-2

95 spike protein when expressed on its own, outside the context of an infected cell, and also

96 in the context of SARS-CoV-2 infected cells. These and other results raise the possibility

97 that that a single, lysosome-related mechanism may explain the pleiotropic effects of the

98 D614G mutation on spike protein biogenesis, accelerated virus entry, and enhanced

99 infectivity.

100

Results

Validating IFM-based SARS-CoV-2 serology tests

Fluorescence microscopy offers many advantages as a serology test platform, including high sensitivity, broad dynamic range, use of proteins in their native conformation and biological context, ability to incorporate in-sample controls that minimize false positive and false negative results, and the potential to interrogate multiple antibody responses in a single sample. As a first step towards the development of such an assay for SARS-CoV-2 antibodies, we generated cell lines designed to express the SARS-CoV-2 nucleocapsid, spike, or membrane proteins in response to doxycycline. These Htet1/N, Htet1/S**, and Htet1/M cell lines were subjected to immunoblot analysis, which confirmed that each cell line expressed its cognate SARS-CoV-2 protein in response to doxycycline (**supplemental figure S1**). It should be noted that S** corresponds to full-length spike that carries a pair of trimer-stabilizing proline mutations (986KV987 to 986PP987) and a quartet of substitutions at the S1/S2 protease cleavage site (682RRAR685 to 682GSAG685), a form of spike that displays the prefusion conformation (Wrapp et al., 2020) and may therefore be particularly effective at capturing neutralizing anti-spike antibodies.

We next seeded Htet1/N, Htet1/S**, and Htet1/M cells into 96-well glass-bottom tissue culture plates along with ~10% Htet1 cells (to serve as an internal negative control), incubated the cells overnight in doxycycline-containing media, and then processed these cells for immunofluorescence microscopy. In this format, the fixed adherent cells serve

7

124   as a solid support for capturing anti-SARS-CoV-2 antibodies from patient plasmas, the

125   presence of human antibodies bound to the viral protein is detected using fluorescently-

126   tagged donkey antibodies specific to human immunoglobulins (IgG, IgM, and IA),

127   mCherry identifies the viral protein-expressing cells, and DAPI stains the nucleus. When

128   these cells were tested using 40 control plasmas (all collected prior to the COVID-19

129   pandemic), we failed to detect any specific reaction to the N, S** or M proteins (**Fig. 1,**

130   **top row**; **supplemental figures S2-S5**).

131

132   In contrast, plasmas from hospitalized, PCR-confirmed, COVID-19 patients (collected on

133   day 0 of admittance into Johns Hopkins Hospital during April 2020) displayed a variety of

134   reactivities towards the N, S**, and M proteins. Of the 30 COVID-19 patient plasmas that

135   were tested, 23 (~3/4) contained antibodies that bound to N-expressing cells, 20 (~2/3)

136   contained antibodies that bound to S**-expressing cells, and 13 (~1/2) scored positive for

137   the presence of anti-M antibodies (**Fig. 1, rows 2-6**; **supplemental figures S6, S7**).

138   Moreover, all plasmas with anti-M antibodies also contained anti-N and anti-S antibodies

139   (**Table 1**). These results establish the validity of microscopy-based serology testing,

140   indicate that the levels of anti-M antibodies may be a more reliable indicator of a deep

141   and broad antibody responses to SARS-CoV-2 infection, and are generally consistent

142   with prior studies of COVID-19 patient antibody responses (Grzelak et al., 2020; Whitman

143   et al., 2020),

144

145   ***Patient antibodies reveal an antigenically distinct subpopulation of spike***

146   The SARS-CoV-2 spike protein is known to oscillate between multiple conformational

147   states (Ke et al., 2020) and the anti-spike antibody responses of COVID-19 patients may

148   allow us to detect functionally significant fluctuations in spike protein confirmation within

149   its native context of the human cell. Given that the 986KV987 to 986PP987 and

150   682RRAR685 to 682GSAG685 substitutions present in the S** protein are designed to

151   limit such conformational fluctuations (Wrapp et al., 2020), we developed cell lines that

152   express functional forms of spike. Htet1/S^{W1} was engineered to express the spike protein

153   encoded by the Wuhan-1 isolate of SARS-CoV-2 (Zhou et al., 2020) and was probed with

154   plasmas with a small subset of COVID-19 patients (i.e. E12, E9, 5, and G4). Some of

155   these plasmas (plasmas E12 and E9) generated an antibody staining pattern against the

156   S^{W1} protein that conformed to the expected distribution, namely strong staining at the

157   plasma membrane and in some cells in the Golgi, shown here by the occasional co-

158   localization with GM130 (*Fig. 3, left column*). However, staining with other plasmas (5,

159   G4) allowed the detection of yet another subpopulation of spike proteins within large, non-

160   Golgi, intracellular structures.

161

162   These results indicate that spike expression in human cells leads to the creation of

163   antigenically distinct subpopulations of spike that display different subcellular

164   distributions, and furthermore, that COVID-19 patients vary significantly in their

165   development of antibodies to these different conformations. In light of these findings, we

166   tested whether plasma antibodies might shed light on the effects of the spike D614G

167   mutation, which is known to enhance viral fitness through an increase in SARS-CoV-2

168   infectivity and transmission (Hou et al., 2020; Korber et al., 2020; Lorenzo-Redondo et

169   al., 2020). Towards this end, we generated the Htet1/S^{D614G} cell line and interrogated

170   S^{D614G}-expressing cells using the same four plasmas (**Fig. 3, right column**). Although

171   this form of spike differs from S^{W1} by just a single amino acid, all four plasmas revealed

172   enhanced staining of spike in these large, non-Golgi intracellular compartments, raising

173   the possibility that the D614G mutation either enhances the trafficking of spike to these

174   compartments or enhances a conformational shift that allows its detection by the

175   antibodies in these plasmas.

176

177   ***SARS-CoV-2 spike is trafficked to lysosomes***

178   Given the central role of spike in SARS-CoV-2 biology, the pronounced impact of the

179   D614G mutation on the COVID-19 pandemic, and the fact that all leading vaccine

180   candidates are based solely on spike, we sought to determine the identity of these large,

181   spike-containing structures. This was done by inducing Htet1/S^{D614G} cells to express

182   spike and then processing the cells for immunofluorescence microscopy using plasma

183   G4 and antibodies directed against marker proteins of various subcellular compartments.

184   These experiments showed no labeling of these structures with markers of the ER

185   (calnexin and BiP), the ERGIC (ERGIC53 and ERGIC3,) the Golgi (GM130), endosomes

186   (EEA1) or the plasma membrane (CD810 (**supplemental figure S8**). However, these

187   structures did label with antibodies specific for lysosomal membrane markers Lamp1 and

188   Lamp2 (**Fig. 3A, B**) and the lysosome-associated proteins Lamp3 (CD63) and mTOR

189   (**Fig. 3C, D**). It has recently been shown that MHV-infected cells mislocalize the KDEL

190   receptor (KDELR) from the ER and Golgi to the lysosome as part of virus-mediated

191   reprogramming of host secretory pathways (Ghosh et al., 2020), and we observed that

192   spike expression induced a redistribution of the KDEL receptor to the lysosome in a

193   portion of spike-expressing cells (**Fig. 3E**).

194

195   These experiments revealed that lysosomes of spike-expressing cells accumulated in

196   large clusters, a phenotype that was relatively uncommon in non-expressing cells. This

197   appearance is likely due to lysosome clustering rather than lysosome fusion, and to test

198   this hypothesis we examined S^{D614G} and Lamp2 distibution following a brief exposure to

199   vacuolin-1, a PIKfyve inhibitor known to induce lysosome swelling (Huynh and Andrews,

200   2005; Sano et al., 2016). As expected, cells treated with vacuolin-1 contained swollen

201   lysosomes several micrometers in diameter (**Fig. 4A-C**). Importantly, the membranes of

202   these swollen lysosomes were labeled for both S^{D614G} and Lamp2, confirming that these

203   proteins were indeed co-localized in lysosome membranes. Moreover, the sizes and

204   numbers of these lysosomes appeared to be similar in expressing and non-expressing

205   cells, indicating that spike expression induces lysosome clustering rather than lysosome

206   fusion.

207

208   ***Spike expression disrupts lysosome function***

209   Lysosomes are the terminal destination for materials brought into the cell by fluid-phase

210   endocytosis (Braulke and Bonifacino, 2009), a process that can be monitored by

211   incubating cells with fluorescently-labeled, high molecular weight dextrans (Ohkuma,

212   1989). To determine whether spike-containing lysosomes retained this core function of

213   lysosomes, we incubated Htet1/S^{D614G} cells with Alexa Fluor-647-labeled dextran (~10

214   kDa), followed by a 3-hour chase in label-free media to allow endocytosed material to

215   reach the lysosome. Furthermore, we performed these experiments on cells that had only

216   been induced to express spike for 20 hours rather than several days, to increase the

217   probability that we visualize cells at an earlier stage of lysosome clustering when

218   individual lysosomes could still be resolved. This presumption was borne out by the

219   extensive co-localization of spike and Lamp2 in small lysosomes scattered throughout

220   the cytoplasm of control Htet1/S^{D614G} cells (**Fig. 4D**). As for whether spike-containing

221   lysosomes were able to accumulate A647-dextran uptake similarly to other lysosomes in

222   the cell, or in other cells, we observed that spike-containing lysosomes displayed little if

223   any A647-dextran fluorescence, even in cells that contained many spike-negative, A647-

224   dextran-positive lysosomes (**Fig. 4E, F**). Interestingly, both populations of lysosomes

225   within these cells (spike+, A647- and spike-, A647+) appeared to cluster together in cells

226   that had larger lysosome clusters.

227

228   Lysosome acidification is another hallmark of lysosome function, and is catalyzed by the

229   vacuolar ATPase (V-ATPase) proton pump (Futai et al., 2019). A number of probes have

230   been developed that label acidic compartments (Chazotte, 2011), including the

231   lysotracker series of probes. To determine whether spike-containing lysosomes have a

232   pH similar to spike-negative lysosomes, we labeled Htet1/S^{D614G} cells with Lysotracker

233   Deep Red and then processed the cells for immunofluorescence microscopy using

234   plasma G4 to detect the lysosomal forms of spike. Lysotracker Deep Red labeled many

235   lysosomes brightly, and while some spike-containing lysosomes displayed labeling

236   consistent with an acidic lumen, many of the spike-containing lysosomes displayed

237   relatively low or no lysotracker fluorescences (**Fig. 4G**).

238

Spike trafficking to lysosomes is resistant to inhibitors of endocytosis, microtubules, and secretion but sensitive to V-ATPase inhibition

241   Proteins can be trafficked to lysosomes following endocytosis from the plasma membrane

242   by a pathway that often effects their destruction, or by direct intracellular vesicle traffic

243   (Braulke and Bonifacino, 2009). To determine whether the lysosomal trafficking of spike

244   occurs via the endocytic pathway so often associated with cargo protein destruction, we

245   incubated Htet1/S^{D614G} cells with doxycycline for 14 hours in the presence of vehicle alone

246   (DMSO) or in media containing either of two inhibitors of endocytosis, the dynamin-1

247   inhibitor dynasore, which blocks clathrin-dependent endocytosis (Kirchhausen et al.,

248   2008), or the clathrin inhibitor pitstop2, which blocks both clathrin-dependent and clathrin-

249   independent endocytosis (Dutta et al., 2012). Htet1/S^{D614G} cells incubated with vehicle

250   alone (DMSO) localized spike to Lamp2-positive lysosomes (***Fig. 5A***) and the same was

251   observed for Htet1/S^{D614G} cells incubated with either dynasore or pitstop2 (***Fig. 5B, C***).

252

253   The microtubule-inhibitor nocodazole, while not a general inhibitor of endocytosis, has

254   been shown to impair the lysosomal uptake of selected endocytosed proteins (Tacheva-

255   Grigorova et al., 2013). Moreover, it is known to affect lysosome function by blocking

256   microtubule-dependent retrograde and anterograde movements of lysosomes

257   (Cabukusta and Neefjes, 2018). Addition of nocodazole had no discernable effect on the

258   lysosomal sorting of spike (***Fig. 5D***) and while it had some effect on lysosome distribution,

259   it did not prevent spike-induced lysosome clustering. Lysosome function is more severely

260   inhibited by bafilomycin A1, a potent inhibitor of the V-ATPase that blocks acidification of

261   lysosomes (and other organelles), prevents the maturation of many lysosomal

262   hydrolases, and inhibits the activity of many pH-dependent lysosomal enzymes. and

263   required for lysosome acidification (Braulke and Bonifacino, 2009; Futai et al., 2019). To

264   explore its effects on the lysosomal sorting of spike, cells were incubated with bafilomycin

265   throughout the period of spike induction and then processed for immunofluorescence

266   microscopy. Bafilomycin-treated cells localized spike to Golgi and plasma membranes

267   rather than lysosomes (**Fig. 5F-I**), demonstrating that the trafficking of spike to lysosomes

268   is a V-ATPase-dependent process. Interestingly, the lysosomes of bafilomycin-treated

269   cells showed little if any clustering.

270

271   ***The D614G mutation enhances the lysosomal sorting of spike***

272   Given that the D614G mutation has a significant impact on SARS-CoV-2 infectivity and

273   transmission, we asked whether this mutation might impact the lysosomal sorting of spike.

274   Htet1/S^{W1} and Htet1/S^{D614G} cells express spike in response to doxycycline, and at similar

275   levels (**Fig. 6A**). Significant amounts of spike are proteolytically processed at its

276   682RRAR685 motif to generate the S2 and S1 fragments, and these cells also contained

277   similar levels of both S2 and S1. However, the D614G mutation did induce a slight shift

278   in the relative extent of processing at the S1/S2 boundary, shown here by somewhat less

279   full-length spike in Htet1/S^{D614G} cells relative to Htet1/S^{W1} cells.

280

281   To determine the subcellular distribution of the D614 and G614 forms of spike,

282   doxycycline-induced Htet1/S^{W1} and Htet1/S^{D614G} cells were processed for

283   immunofluorescence microscopy using an antibody that binds the C-terminal 14 amino

14

284   acids of spike (-DSEPVLKGVKLHYT$_{COOH}$), a region of the protein that is shielded by a

285   lipid bilayer from the D614G mutation and the conformational changes it might induce.

286   Although both forms of spike displayed significant co-localization with the lysosomal

287   marker Lamp2, the D614G mutation appeared to induce a shift in spike protein sorting

288   towards the lysosome (**Fig. 6B, C**). Although the relative amounts of lysosome-localized

289   spike varied significantly from one cell to another in both cell populations, digital image

290   analysis quantified the effect of the D614G mutation as 54% increase in its lysosomal

291   staining (p = 0.00000024; Student's t-test; 2-tailed; two-sample, unequal variance), from

292   an average of 817 +/- 44 (standard error of the mean (s.e.m.)) in Htet1/S^{W1} cells (n = 34

293   images) to an average of 1265 +/- 64 (s.e.m) in Htet1/S^{D614G} cells (n = 37 images) (**Fig.**

294   **6D**).

295

296   These results suggest a model of SARS-CoV-2 biogenesis in which the D614G mutation

297   enhances spike protein trafficking to the lysosome. Given the recent report that the

298   biogenesis of newly-synthesized MHV particles occurs via lysosomes and that MHV-

299   infected cells accumulate MHV particles in lysosomes (Ghosh et al., 2020), we tested

300   whether the D614G mutation might promote the lysosomal accumulation of spike and

301   spike-containing vesicles in SARS-CoV-2-infected cells. More specifically, we infected

302   VeroE6TMPRSS2 cells with equal m.o.i. of a G614 strain of SARS-CoV-2 (HP7) or a

303   D614 strain of SARS-CoV-2 (HP76). 18 hours after initiation of infection, the two cell

304   populations were fixed, permeabilized, and processed for confocal immunofluorescence

305   microscopy using antibodies specific for spike and Lamp2 (**Fig. 7**). In cells infected with

306   the G614 virus, spike was localized primarily to small intracellular vesicles clustered in

307   the perinuclear area of the cell, proximal to Lamp2-positive structures, often co-localizing

308   with Lamp2, and especially in small, virus-sized punctae surrounded by Lamp2-positive

309   membrane (**Fig. 7A-D**). In contrast, spike distribution in D614 virus-infected cells was

310   distributed across a much broader array of intracellular compartments, especially the

311   plasma membrane and intracellular compartments distant from Lamp2-positive structures

312   (**Fig. 7E-H**). However, these differences were a matter of degree, as D614 spike also

313   displayed some labeling in Lamp2-positive and nearby compartments, as well as in small

314   spike-positive puncta surrounded by Lamp2-containing membrane.

315

Discussion

We show here that the spike D614G mutation alters spike protein sorting, enhancing its trafficking towards the lysosome and away from other intracellular compartments. This D614G-induced shift in spike protein trafficking was observed in human cells expressing the spike protein on its own, outside the context of a viral infection, where it appeared to enhance spike-induced lysosomes clustering. It was also observed in the context of SARS-CoV-2-infected cells, as spike protein encoded by G614 virus displayed increased association with lysosomes and reduced accumulation in non-lysosomal compartmets and areas of the cell. Furthermore, we observed that cells infected by a G614 strain of SARS-CoV-2 exhibited an enhanced accumulation of discrete, small, spike-containing punctae within Lamp2-positive membranes. In addition, we observed that the D614G mutation induced a slight elevation in spike protein processing at the S1/S2 junction. To the best of our knowledge, the D614G-induced lysosomal shift in spike protein trafficking and slight elevation in spike processing represent the earliest cell biological and biochemical manifestations of the D614G mutation, raising the strong possibility that they may contribute to the pronounced effects of the D614G mutation on SARS-CoV-2 infectivity, viral load, and transmission (Hou et al., 2020; Korber et al., 2020; Lorenzo-Redondo et al., 2020).

Numerous lines of evidence support our conclusion that spike is trafficked to the lysosome membrane, including its co-localization with Lamp1, Lamp2, and Lamp3/CD63, its ring-like staining in vacuolin-1-treated cells, its induction of lysosome clustering, and its lysosomal localization when detected with a relatively conformation-independent antibody

17

339   probe (the affinity purified antibodies to its C-terminal 14 amino acids. As for how spike is

340   trafficked to lysosomes, our data indicate that it can occur independently of endocytosis,

341   as it's lysosomal accumulation was not blocked by inhibitors of clathrin-dependent or

342   clathrin-independent endocytosis. Spike trafficking to lysosomes was also unaffected by

343   the microtubule depolymerizing agent nocodazole, even though nocodazole ablates

344   motor-directed lysosome movements. Spike trafficking to lysosomes was, however,

345   strongly inhibited by bafilomycin A1, a V-ATPase inhibitor, indicating that compartment

346   acidification is critical to the lysosomal trafficking of spike. These results are consistent

347   with those from a recent CRISPR-based screen for genes required for SARS-CoV-2

348   replication, which identified 13 components of the V-ATPase among the 50-most

349   important genes for SARS-CoV-2 replication (Daniloski et al., 2020).

350

351   In addition to being trafficked to lysosomes, the expression of spike appears to alter

352   lysosome function. This was apparent from the fact that spike expression induces a

353   pronounced clustering of lysosomes, especially in cells expressing the G614 form of spike

354   (*Table 2*). While we do not know the molecular mechanism by which spike expression

355   drives lysosome clustering, it appeared to be a microtubule-independent process, as it

356   was not inhibited by nocodazole, similar to previous studies of lysosome clustering (Ba et

357   al., 2018). Spike-induced alteration of lysosome function was also apparent from was the

358   fluorescent dextran uptake experiments, which revealed that spike-containing lysosomes

359   were defective in uptake of this fluid-phase endocytosis marker, and may also display a

360   somewhat reduced ability to acidify their lumen, as some spike-containing lysosomes

361   displayed low labeling with Lysotracker Deep Red.

18

362

363   Given that the D614G mutation enhances viral fitness, it is important to consider how viral

364   fitness might be promoted by an increase in the lysosomal sorting of spike and the

365   accumulation of spike-containing punctae within lysosomes of SARS-CoV-2-infected

366   cells. The most obvious possibility is that these changes facilitate the lysosomal phases

367   of SARS-CoV-2 virion biogenesis. This conclusion is based in part on the recent report

368   by Ghosh et al that MHV is released independently of the biosynthetic secretory pathway,

369   that MHV virions accumulate in lysosomes, that MHV release is an Arl8-dependent

370   lysosomal secretory pathway, and that SARSW-CoV-2 virions accumulate in a lysosome-

371   like structure of SARS-CoV-2-infected cells (Ghosh et al., 2020). This model of

372   coronavirus egress involves some degree of aberration to protein egress in general, as

373   MHV infection induced the lysosomal trafficking of the KDEL receptor (Ghosh et al.,

374   2020), a phenotype that we observed for spike-expressing cells.

375

376   An analysis of matched D614 and G614 SARS-CoV-2 virions revealed no difference in

377   the ultrastructure of SARS-CoV-2 particles, the shape of spike trimers, or the amounts of

378   S and S2 in viral particles (Hou et al., 2020), while Zhang et al. (doi:

379   10.1101/2020.06.12.148726) concluded that the D614G mutation led to enhanced

380   retention of S1. Our data show that cells expressing matched D614 and G614 forms of

381   spike show no difference in the amounts of cell-associated S1 and S2, though there may

382   be a slightly lower amount of full-length S. This may reflect a slight increase in the

383   cleavage of G614 spike at the S1/S2 boundary, and since lysosomal proteases can

384   catalyze this event it may be a consequence of enhanced lysosomal sorting of D614G

385   spike proteins. Alternatively, enhanced spike cleavage by Golgi proteases such as furin

386   may potentiate the lysosomal sorting of spike.

387

388   The most obvious effect of the D614G mutation is the ~4-8-fold increase in a proxy marker

389   of SARS-CoV-2 infection (an encoded luciferase) at 8 hours post-infection (Hou et al.,

390   2020), suggestive of accelerated viral entry. Although it is at least formally possible that

391   these various effect of the D614G mutation are unrelated, the more parsimonious

392   hypothesis is that they are all reflections of a common mechanism. As for what this

393   mechanism might be, there is already extensive precedent from the field of lysosomal

394   protein sorting. Specifically, the mannose-6-phosphate (M6P)-M6P receptor system

395   mediates the lysosomal delivery of both newly-synthesized intracellular cargoes and

396   endocytosed cargoes retrieved from the extracellular milieu (Braulke and Bonifacino,

397   2009). Although there is a report of M6P modification on spike glycans (Brun et al. 2020

398   https://www.biorxiv.org/content/10.1101/2020.11.16.384594v1.full.pdf), we do not

399   suggest that the effects of the D614G mutation are necessarily mediated by M6P

400   receptors. Rather, we posit the more general hypothesis that spike protein interactions

401   with one or more cell surface proteins accelerate SARS-CoV-2 entry and that the same

402   or similar interactions facilitate the lysosomal trafficking of newly-synthesized spike

403   proteins, perhaps by interactions with newly-synthesized versions of the same spike-

404   binding proteins in the ER, ERGIC, or Golgi. In light of this hypothesis, it is interesting to

405   note that SARS-CoV-2 infection is exquisitely sensitive to a known inhibitor of plasma

406   membrane-to-lysosome traffic (Kang et al., 2020) and that SARS-CoV-2 infection requires

407   numerous proteins involved in lysosome biology (Daniloski et al., 2020).

408   **Materials and Methods**

409

410   **Cell lines, cell culture, transfections**

411   HEK293 cells (ATCC) were cultured in complete medium (DMEM containing 10% fetal

412   bovine serum and 1% penicillin/streptomycin solution (10,000 units/ml)). Transfections

413   were carried out using lipofectamine according to the manufacturer's instructions. Htet1

414   cells were generated by transfecting HEK293 cells with the plasmid pS147, which

415   encodes the tetracycline-activated transcription factor rtTAv16 (Zhou et al., 2006),

416   followed by selection of zeocin-resistant transgenic cell clones (200 ug/ml zeocin), and

417   pooling of these clones. SARS-CoV-2 protein-expressing cell lines were generated by

418   transfection of Htet1 cells with Sleeping Beauty transposons carrying a tet-regulated

419   transgene designed to express each SARS-CoV-2 protein under control of the

420   doxycycline-regulated TRE3G promoter. One to two days after transfection, cells were

421   placed in selective media containing 1 ug/ml puromycin and 200 ug/ml zeocin. Multiple

422   clones were obtained from each transfection, pooled, and expanded to create master

423   banks of each test line. Expression of SARS-CoV-2 protein was induced by adding

424   doxycycline to the culture medium at a final concentration of 1 ug/ml.

425

426   **Plasmids**

427   The plasmid pS147 is a CMV-based vector designed to express the rtTAv16 protein from

428   a polycistronic ORF, upstream of a viral 2a peptide and the Bleomycin resistance coding

429   region. Other vectors used in this study were based on a Sleeping Beauty transposon

430   vector (pITRSB) in which genes of interest can be inserted between the left and right

21

431   inverted tandem repeats (ITRs). These include three plasmids in which the region

432   between the ITRs contains (a) one gene in which a crippled EF1alpha promoter drives

433   expression of a polycistronic ORF encoding mCherry, the p2a peptide, and the

434   puromycin-resistance protein, and (b) a second gene in which the TRE3G promoter drives

435   expression of codon-optimized forms of the N, S**, or M proteins (pCG217, pCG218, and

436   pCG221, respectively, which were used to create the Htet1/N, Htet1/S**, and Htet1/M cell

437   lines). Two additional transposon-mobilizing plasmids were also used in this study. These

438   plasmids carry (a) one gene in which a crippled EF1alpha promoter drives expression of

439   the puromycin-resistance protein, and (b) a second gene in which the TRE3G promoter

440   drives expression of codon-optimized forms of the S^{W1} or S^{D614G} proteins (pCG145 and

441   pCG200, respectively, used to create the Htet1/ S^{W1} and Htet1/ S^{D614G} cell lines). All

442   plasmid sequences are available upon request. S** encodes the same protein as S^{W1},

443   with the exception of 6 amino acid changes (986KV987 to 986PP987 and 682RRAR685

444   to 682GSAG685). S^{D614G} encodes the same protein as S^{W1}, with the exception of the

445   D614G amino acid substitution.

446

447   **Immunoblot**

448   HEK293 cell lines were grown in the presence or absence of doxycycline, lysed by

449   addition of sample buffer, separated by SDS-PAGE, transferred to PVDF membranes,

450   and incubated with primary antibodies and HRP-conjugated secondary antibodies.

451   Following extensive washes, proteins were membranes visualized using

452   chemiluminescence reagents and an Amersham Imager 600 gel imaging system.

453

454 **Immunofluorescence microscopy,**

455 Cells were cultured on either sterile, poly-L-lysine-coated coverglasses, or sterile, poly-L-

456 lysine-coated, glass-bottom, black-walled 96 well plates. For serology testing, SARS-

457 CoV-2 protein-expressing cells were mixed with the parental Htet1 cell line at a ratio of

458 ~90%:10%. Cells were exposed to 1 ug/ml doxycycline for 1 day to induce SARS-CoV-2

459 protein expression. Cells were then fixed (4% formaldehyde in PBS), permeabilized (1%

460 Triton X-100 in PBS), and processed for immunofluorescence microscopy using

461 established protocols. Coverglasses were mounted on slides using Fluoromount G

462 (catalog #17984-25 , Electron Microscopy Sciences). Stained cells were visualized using

463 an EVOSM7000 fluorescence microscope (ThermoFisher) equipped with 20x (PL FL 20X,

464 0.50NA/2.5WD), 40x (PLAN S-APO 40X, NA0.95, 0.18MM), and 60x (OBJ PL APO 60X,

465 1.42NA/0.15WD) Olympus objectives) Confocal fluorescence microgaphs were acquired

466 using a Zeiss LSM800 microscope with gallium-arsenide phosphide (GaAsP) detectors

467 and a 100x/1.4na Plan-Apochromat objective. Images were assembled into figures using

468 Adobe Illustrator. Quantitative analysis of image files was performed using ImageJ and

469 proprietary software.

470

471 **Antibodies and other reagents**

472 Rabbit polyclonal antibodies were raised against synthetic peptides corresponding to

473 carboxy-terminal peptides of SARS-CoV-2 N (-KQLQQSMSSADSTQA$_{COOH}$) and S (-

474 DSEPVLKGVKLHYT$_{COOH}$). Rabbit antibodies to the SARS M protein carboxy-terminal

475 peptide (-DHAGSNDNIALLVQ$_{COOH}$) were a gift from C. Machamer, Johns Hopkins

476 University. ThermoFisher was the source for rabbit antibodies directed against LAMTOR1

477   (#8975S), ERGIC3 (#16029-1-AP), ERGIC53 (#13364-1-AP), and calnexin (#PA5-

478   34665) and for mouse monoclonal antibodies to EEA1 (#48453) and Lamp2 (MA1-205).

479   Rabbit antibodies to mTOR were obtained from Cell Signaling (#2972S). Mouse

480   monoclonal antibodies to GM130 (#610822) and CD81 (#555675) were obtained from

481   BD. Mouse monoclonal antibody to Lamp3/CD63 (#NBP2-32830) was obtained from

482   Novus. Mouse monoclonal antibody directed against CD9 (#312102) was obtained from

483   BioLegend. Rabbit polyclonal antibodies to BiP/GRP78 (#21685) and mouse monoclonal

484   to Lamp1 (#24170) were from Abcam. Fluorescently labeled secondary antibodies

485   specific for human Igs (IgG, IgM, and IgA; pan Ig), human IgG, rabbit IgG, or mouse IgG

486   were obtained from Jackson ImmunoResearch. Lysotracker Deep Red (#L12492) and

487   Alexa647-Dextran 10,000 MW (#D22914) were obtained from ThermoFisher. We thank

488   Dr. Nihal Altan-Bonnet for generous gift of the anti-BiP/GRP78 antibodies, the Lamp1

489   monoclonal, and polyclonal antibody to the KDEL receptor.

490

491   **Human Plasmas**

492   All patient plasmas were collected using standard procedures for blood draw and plasma

493   collection. Following Johns Hopkins Medicine Institutional Review Board (IRB) approval,

494   plasma samples were obtained under informed consent from healthy donors prior to the

495   COVID-19 pandemic (JHM IRB NA_0004638) as described (Cox et al., 2005). The

496   COVID-19 specimens utilized for this publication were obtained from the Johns Hopkins

497   Biospecimen Repository, which is based on the contribution of many patients, research

498   teams, and clinicians, and were collected following IRB approval (Johns Hopkins COVID-

499   19 Clinical Characterization Protocol for Severe Infectious Diseases (IRB00245545) and

500   Johns Hopkins COVID-19 Remnant Specimen Repository (IRB00248332)). All COVID-

501   19 patient plasmas used in this study were collected on the day of admission of the patient

502   into the Johns Hopkins Hospital, and between the dates of April 7 and April 22, 2020.

503

504

505   **Virus and virus infections**

506   VeroE6TMPRSS2 cells (Matsuyama et al., 2020) were used to grow and titrate infectious

507   virus using established protocols (Klein et al., 2020; Schaecher et al., 2007). The clinical

508   isolates SARS-CoV-2/USA/MD-HP00076/2020 (Spike D614; GenBank: MT509475.1)

509   and SARS-Cov-2/USA/DC-HP00007/2020 (Spike G614; GenBank: MT509464.1) were

510   isolated using published procedures (Gniazdowski et al., 2020) and virus stocks were

511   grown on VeroE6TMPRSS2 cells. Virus stocks were sequenced to confirm that the amino

512   acid sequence of the isolate was identical to the sequence derived from the clinical

513   sample.

535

Figure Legends

Figure 1. Microscopy-based serology. Fluorescence micrographs of (left two columns) Htet1/N, (middle two columns) Htet1/S**, and (right two columns) Htet1/M cells that had been processed for immunofluorescence using human plasmas from (row 1) a control patient and (rows 2-6) 5 different COVID-19 patients. Bound antibodies were detected using Alexafluor 488-conjugated anti-human Ig antibodies, DAPI was used to stain the nucleus, and mCherry was expressed from the same transposon as the viral protein. The left column in each pair shows the merge of all three images while the right column of each pair shows the staining observed for the patient plasma antibodies. Bar, 75 μm.

Figure 2. Human plasmas reveal differential trafficking of antigenically distinct forms of spike. Fluorescence micrographs of (left column) Htet1/S^{W1} cells and (right column) Htet1/S^{D614G} stained with (green) plasmas from COVID-19 patients E12, E9, 5, and G4, as well as with (red) antibodies specific for the Golgi marker GM130, and (blue) DAPI. White arrowheads point to large, spike-containing intracellular compartments that lack GM130. Insets (~2.5-fold higher magnification) show greater detail in areas of particular interest. Bar, 50 μm.

Figure 3. SARS-CoV-2 spike is trafficked to lysosomes. Fluorescence micrographs of Htet1/S^{D614G} cells induced with doxycycline and processed for immunofluorescence microscopy using (blue) DAPI, (green) plasma from COVID-19 patient G4, and (red) antibodies specific for for (A) Lamp1, (B) Lamp2, (C) Lamp3/CD63, (D) mTOR1, and (E)

559   KDEL receptor (KDEL-R). White arrowheads denote the positions of S^{D614G}-containing

560   lysosome-related compartments. Insets (~3-fold higher magnification) show greater detail

561   in areas of particular interest. Bar, 50 μm.

562

563   ***Figure 5. Spike expression induces lysosome clustering and inhibits lysosome***

564   ***function***. (A-C) Micrographs of Htet1/S^{D614G} cells induced with doxycycline for two days

565   followed by treatment with (A) DMSO or (B, C) vacuolin-1 for 3 hours. Cells were stained

566   with (green) COVID-19 patient plasma G4, (red) a monoclonal anti-Lamp2 antibody, and

567   (blue) DAPI. (D-F) Micrographs of Htet1/S^{D614G} cells induced with doxycycline for 20

568   hours (D) without treatment, (E) incubated with Alexa Fluor 647-dextran for an additional

569   3 hours in media containing doxycycline but lacking Alexa Fluor 647-dextran, or (F)

570   incubated for one hour in media containing both doxycycline and Lysotracker Deep Red.

571   Cells were stained with (green) COVID-19 patient plasma G4 and (red) a monoclonal

572   anti-Lamp2 antibody. Insets (~3-fold higher magnification) show greater detail in areas of

573   particular interest. Bar, 50 μm.

574

575   ***Figure 6. The D614G mutation enhances lysosomal sorting of spike***. (A) Immunoblot

576   analysis of doxycycline-treated Htet1, Htet1/S^{W1}, and Htet1/S^{D614G} cells. Cell lysates were

577   prepared and separated by SDS-PAGE, then processed for immunoblot using (left panel)

578   affinity purified antibodies specific for the C-terminal 14 amino acids of spike, (center

579   panel) a mouse monoclonal antibody specific directed against the S1 region of spike, and

580   (right panel) endogenously expressed Hsp90. (B, C) Fluorescence micrographs of

581   doxycycline-treated Htet1/S^{W1} and Htet1/S^{D614G} cells stained with (green) affinity purified

582   antibodies specific for the C-terminal 14 amino acids of spike, (red) a mouse monoclonal

583   antibody specific for Lamp2, and (blue) DAPI. The upper panels (merge) display the

584   composite of all three images, above the individual images for (green) spike and (red)

585   Lamp2. Insets (~3-fold higher magnification) show greater detail in areas of particular

586   interest.   Bar, 50 μm. (D) Plot of lysosome-associated levels of spike (relative mean

587   fluorescence, arbitrary units) in cells expressing S^{W1} or S^{D614G}.

588

589   ***Figure 7. G614 and D614 spike in SARS-CoV-2-infected cells***. Confocal fluorescence

590   micrographs of Vero/TMPRSS2 cells infected with (A-D) a spike G614 strain of SARS-

591   CoV-2 or (E-H) a spike D614 strain of SARS-CoV-2. Cells were infected with equal

592   amounts of virus, incubated for 18 hours, then fixed, permeabilized, and stained with

593   (green) affinity purified antibodies specific for the C-terminal 14 amino acids of spike, (red)

594   a monoclonal anti-Lamp2 antibody, and (blue) DAPI. Insets (~3-fold higher magnification)

595   show greater detail in areas of particular interest.   Bar in original images, 10 μm; Bar in

596   magnified insets, 2 μm.

597

598   **Tables**

599   **Table 1. Microscopy-based serology assay results for 30 COVID-19 plasmas.**

Plasma	α-N Ab	α-S Ab	α-M Ab
E5	positive	positive	negative
E6	positive	positive	negative
E7	positive	positive	negative
E8	positive	positive	positive
E9	positive	positive	positive
E10	positive	positive	negative
E11	positive	positive	positive
E12	positive	positive	positive
F1	positive	positive	positive
F2	positive	positive	negative
F3	positive	positive	positive
F4	positive	positive	negative
F5	negative	negative	negative
F7	positive	positive	positive
F8	negative	negative	negative
F9	positive	negative	negative
F10	negative	negative	negative
F11	negative	negative	negative
F12	positive	positive	positive
G1	positive	positive	positive
G2	positive	positive	positive
G3	negative	negative	negative
G4	positive	positive	negative
G5	positive	negative	negative
G6	negative	negative	negative
G7	positive	negative	negative
G8	negative	negative	negative
G9	positive	positive	positive
G10	positive	positive	positive
plasma 5	positive	positive	positive

600

601

602

30

603 **Table 2. Percentage of cells with clustered (Lamp2+) lysosomes**

	Htet1/S^{D614G}	Htet1/S^{W1}	Htet1
1-day doxycycline	33% (21/62)	8% (8/101)	3% (9/355)

604

605   **Legends to Supplemental Figures**.

606

607   *Supplemental figure 1. Doxycycline-inducible expression of SARS-CoV-2 N, S**,*

608   *and M*. Immunoblot of whole cell lysates of Htet1 cells, and of Htet1/N, Htet1/S**, and

609   Htet1/M cells grown in the absence or presence of doxycycline. Blots were probed with

610   (left panel) rabbit polyclonal anti-peptide antibodies specific for SARS-CoV-2 N protein,

611   (center panel) rabbit polyclonal anti-peptide antibodies specific for SARS-CoV-2 S spike

612   protein, and (right panel) rabbit polyclonal anti-peptide antibodies specific for the SARS

613   and SARS-CoV-2 M protein. Size markers, from top: 250 kDa, 150 kDa, 100 kDa, 75 kDa,

614   50 kDa, 37 kDa, 25 kDa, 20 kDa, 15 kDa, 10 kDa. Predicted molecular masses are 46

615   kDa for N, 141 kDa for S**, and 25 kDa for M. The high MW forms of M apparent in these

616   blots were observed whenever M was expressed in isolation.

617

618   *Supplemental figure 2. Control plasma staining data I*. Fluorescence micrographs of

619   doxycycline-induced Htet1/N, Htet1/S**, and Htet1/M cells. Cells were processed for

620   immunofluorescence microscopy and stained to detect (green) bound human plasma Ig

621   and (blue) DAPI, then imaged to detect bound Ig, (red) mCherry, and DAPI. Micrographs

622   present the merge of all three labels and are organized with cell lines in each column and

623   plasmas in each row. These plasmas were collected prior to COVID-19 pandemic. Bar,

624   75 μm.

625

626   *Supplemental figure 3. Control plasma staining data II*. Fluorescence micrographs of

627   doxycycline-induced Htet1/N, Htet1/S**, and Htet1/M cells. Cells were processed for

628   immunofluorescence microscopy and stained to detect (green) bound human plasma Ig

629   and (blue) DAPI, then imaged to detect bound Ig, (red) mCherry, and DAPI. Micrographs

630   present the merge of all three labels and are organized with cell lines in each column and

631   plasmas in each row. These plasmas were collected prior to COVID-19 pandemic. Bar,

632   75 μm.

633

634   ***Supplemental figure 4. Control plasma staining data III***. Fluorescence micrographs of

635   doxycycline-induced Htet1/N, Htet1/S**, and Htet1/M cells. Cells were processed for

636   immunofluorescence microscopy and stained to detect (green) bound human plasma Ig

637   and (blue) DAPI, then imaged to detect bound Ig, (red) mCherry, and DAPI. Micrographs

638   present the merge of all three labels and are organized with cell lines in each column and

639   plasmas in each row. These plasmas were collected prior to COVID-19 pandemic. Bar,

640   75 μm.

641

642   ***Supplemental figure 5. Control plasma staining data IV***. Three-color merged

643   fluorescence micrographs of Htet1/N, Htet1/S**, and Htet1/M cells imaged for (green)

644   human plasma Ig staining, (red) mCherry expression and (blue) DAPI. Micrographs are

645   organized with cell lines in each column, and plasmas in each row. These plasmas were

646   collected prior to COVID-19 pandemic. Bar, 75 μm.

647

648   ***Supplemental figure 6. COVID-19 plasma staining data I***. Three-color merged

649   fluorescence micrographs of Htet1/N, Htet1/S**, and Htet1/M cells imaged for (green)

650   bound human plasma Ig, (red) mCherry expression and (blue) DAPI. Micrographs are the

651 merge of all three images and are organized with cell lines in each column, and plasmas

652 in each row. These plasmas were collected from COVID-19 patients on their first day of

653 admittance into Johns Hopkins Hospital in April 2020. Bar, 75 μm.

654

655 ***Supplemental figure 7. COVID-19 plasma staining data II***. Three-color merged

656 fluorescence micrographs of Htet1/N, Htet1/S**, and Htet1/M cells imaged for (green)

657 bound human plasma Ig, (red) mCherry expression and (blue) DAPI. Micrographs are the

658 merge of all three images and are organized with cell lines in each column, and plasmas

659 in each row. These plasmas were collected from COVID-19 patients on their first day of

660 admittance into Johns Hopkins Hospital in April 2020. Bar, 75 μm.

661

662 ***Supplemental figure 8***. ***ER, ERGIC, Golgi, endosome, and plasma membrane***

663 ***marker proteins are not enriched in large, spike-containing intracellular***

664 ***compartments***. Fluorescence micrographs of Htet1/S^{D614G} cells induced with

665 doxycycline and processed for immunofluorescence microscopy using (blue) DAPI,

666 (green) plasma G4, and (red) antibodies specific for (A) calnexin, (B) BiP/GRP78, (C)

667 ERGIC53, (D) ERGIC3, (E) GM130, (F) EEA1, and (G) CD81. Bar, 50 μm.

668

References

Ba, Q., Raghavan, G., Kiselyov, K., and Yang, G. (2018). Whole-Cell Scale Dynamic Organization of Lysosomes Revealed by Spatial Statistical Analysis. Cell Rep *23*, 3591-3606.

Braulke, T., and Bonifacino, J.S. (2009). Sorting of lysosomal proteins. Biochim Biophys Acta *1793*, 605-614.

Cabukusta, B., and Neefjes, J. (2018). Mechanisms of lysosomal positioning and movement. Traffic *19*, 761-769.

Cantuti-Castelvetri, L., Ojha, R., Pedro, L.D., Djannatian, M., Franz, J., Kuivanen, S., van der Meer, F., Kallio, K., Kaya, T., Anastasina, M.*, et al.* (2020). Neuropilin-1 facilitates SARS-CoV-2 cell entry and infectivity. Science.

Chazotte, B. (2011). Labeling lysosomes in live cells with neutral red. Cold Spring Harb Protoc *2011*, pdb prot5570.

Coronaviridae Study Group of the International Committee on Taxonomy of, V. (2020). The species Severe acute respiratory syndrome-related coronavirus: classifying 2019-nCoV and naming it SARS-CoV-2. Nat Microbiol *5*, 536-544.

Cox, A.L., Netski, D.M., Mosbruger, T., Sherman, S.G., Strathdee, S., Ompad, D., Vlahov, D., Chien, D., Shyamala, V., Ray, S.C.*, et al.* (2005). Prospective evaluation of community-acquired acute-phase hepatitis C virus infection. Clin Infect Dis *40*, 951-958.

Daly, J.L., Simonetti, B., Klein, K., Chen, K.E., Williamson, M.K., Anton-Plagaro, C., Shoemark, D.K., Simon-Gracia, L., Bauer, M., Hollandi, R.*, et al.* (2020). Neuropilin-1 is a host factor for SARS-CoV-2 infection. Science.

691 Daniloski, Z., Jordan, T.X., Wessels, H.H., Hoagland, D.A., Kasela, S., Legut, M.,

692 Maniatis, S., Mimitou, E.P., Lu, L., Geller, E*., et al.* (2020). Identification of Required Host

693 Factors for SARS-CoV-2 Infection in Human Cells. Cell.

694 Dutta, D., Williamson, C.D., Cole, N.B., and Donaldson, J.G. (2012). Pitstop 2 is a potent

695 inhibitor of clathrin-independent endocytosis. PLoS One *7*, e45799.

696 Futai, M., Sun-Wada, G.H., Wada, Y., Matsumoto, N., and Nakanishi-Matsui, M. (2019).

697 Vacuolar-type ATPase: A proton pump to lysosomal trafficking. Proc Jpn Acad Ser B Phys

698 Biol Sci *95*, 261-277.

699 Ghosh, S., Dellibovi-Ragheb, T.A., Kerviel, A., Pak, E., Qiu, Q., Fisher, M., Takvorian,

700 P.M., Bleck, C., Hsu, V.W., Fehr, A.R*., et al.* (2020). beta-Coronaviruses Use Lysosomes

701 for Egress Instead of the Biosynthetic Secretory Pathway. Cell.

702 Gniazdowski, V., Morris, C.P., Wohl, S., Mehoke, T., Ramakrishnan, S., Thielen, P.,

703 Powell, H., Smith, B., Armstrong, D.T., Herrera, M*., et al.* (2020). Repeat COVID-19

704 Molecular Testing: Correlation of SARS-CoV-2 Culture with Molecular Assays and Cycle

705 Thresholds. Clin Infect Dis.

706 Grzelak, L., Temmam, S., Planchais, C., Demeret, C., Tondeur, L., Huon, C., Guivel-

707 Benhassine, F., Staropoli, I., Chazal, M., Dufloo, J*., et al.* (2020). A comparison of four

708 serological assays for detecting anti-SARS-CoV-2 antibodies in human serum samples

709 from different populations. Sci Transl Med *12*.

710 Hoffmann, M., Kleine-Weber, H., and Pohlmann, S. (2020a). A Multibasic Cleavage Site

711 in the Spike Protein of SARS-CoV-2 Is Essential for Infection of Human Lung Cells. Mol

712 Cell *78*, 779-784 e775.

713 Hoffmann, M., Kleine-Weber, H., Schroeder, S., Kruger, N., Herrler, T., Erichsen, S.,

714 Schiergens, T.S., Herrler, G., Wu, N.H., Nitsche, A.*, et al.* (2020b). SARS-CoV-2 Cell

715 Entry Depends on ACE2 and TMPRSS2 and Is Blocked by a Clinically Proven Protease

716 Inhibitor. Cell *181*, 271-280 e278.

717 Hou, Y.J., Chiba, S., Halfmann, P., Ehre, C., Kuroda, M., Dinnon, K.H., 3rd, Leist, S.R.,

718 Schafer, A., Nakajima, N., Takahashi, K.*, et al.* (2020). SARS-CoV-2 D614G variant

719 exhibits efficient replication ex vivo and transmission in vivo. Science.

720 Huynh, C., and Andrews, N.W. (2005). The small chemical vacuolin-1 alters the

721 morphology of lysosomes without inhibiting Ca2+-regulated exocytosis. EMBO Rep *6*,

722 843-847.

723 Kang, Y.L., Chou, Y.Y., Rothlauf, P.W., Liu, Z., Soh, T.K., Cureton, D., Case, J.B., Chen,

724 R.E., Diamond, M.S., Whelan, S.P.J.*, et al.* (2020). Inhibition of PIKfyve kinase prevents

725 infection by Zaire ebolavirus and SARS-CoV-2. Proc Natl Acad Sci U S A *117*, 20803-

726 20813.

727 Ke, Z., Oton, J., Qu, K., Cortese, M., Zila, V., McKeane, L., Nakane, T., Zivanov, J.,

728 Neufeldt, C.J., Cerikan, B.*, et al.* (2020). Structures and distributions of SARS-CoV-2

729 spike proteins on intact virions. Nature.

730 Kirchhausen, T., Macia, E., and Pelish, H.E. (2008). Use of dynasore, the small molecule

731 inhibitor of dynamin, in the regulation of endocytosis. Methods Enzymol *438*, 77-93.

732 Klein, S.L., Pekosz, A., Park, H.S., Ursin, R.L., Shapiro, J.R., Benner, S.E., Littlefield, K.,

733 Kumar, S., Naik, H.M., Betenbaugh, M.J.*, et al.* (2020). Sex, age, and hospitalization drive

734 antibody responses in a COVID-19 convalescent plasma donor population. J Clin Invest

735 *130*, 6141-6150.

736 Korber, B., Fischer, W.M., Gnanakaran, S., Yoon, H., Theiler, J., Abfalterer, W.,

737 Hengartner, N., Giorgi, E.E., Bhattacharya, T., Foley, B.*, et al.* (2020). Tracking Changes

738 in SARS-CoV-2 Spike: Evidence that D614G Increases Infectivity of the COVID-19 Virus.

739 Cell *182*, 812-827 e819.

740 Lorenzo-Redondo, R., Nam, H.H., Roberts, S.C., Simons, L.M., Jennings, L.J., Qi, C.,

741 Achenbach, C.J., Hauser, A.R., Ison, M.G., Hultquist, J.F.*, et al.* (2020). A Unique Clade

742 of SARS-CoV-2 Viruses is Associated with Lower Viral Loads in Patient Upper Airways.

743 medRxiv.

744 Matheson, N.J., and Lehner, P.J. (2020). How does SARS-CoV-2 cause COVID-19?

745 Science *369*, 510-511.

746 Matsuyama, S., Nao, N., Shirato, K., Kawase, M., Saito, S., Takayama, I., Nagata, N.,

747 Sekizuka, T., Katoh, H., Kato, F.*, et al.* (2020). Enhanced isolation of SARS-CoV-2 by

748 TMPRSS2-expressing cells. Proc Natl Acad Sci U S A *117*, 7001-7003.

749 Ohkuma, S. (1989). Use of fluorescein isothiocyanate-dextran to measure proton

750 pumping in lysosomes and related organelles. Methods Enzymol *174*, 131-154.

751 Poland, G.A., Ovsyannikova, I.G., and Kennedy, R.B. (2020). SARS-CoV-2 immunity:

752 review and applications to phase 3 vaccine candidates. Lancet.

753 Ruch, T.R., and Machamer, C.E. (2012). The coronavirus E protein: assembly and

754 beyond. Viruses *4*, 363-382.

755 Sano, O., Kazetani, K., Funata, M., Fukuda, Y., Matsui, J., and Iwata, H. (2016). Vacuolin-

756 1 inhibits autophagy by impairing lysosomal maturation via PIKfyve inhibition. FEBS Lett

757 *590*, 1576-1585.

758   Schaecher, S.R., Mackenzie, J.M., and Pekosz, A. (2007). The ORF7b protein of severe

759   acute respiratory syndrome coronavirus (SARS-CoV) is expressed in virus-infected cells

760   and incorporated into SARS-CoV particles. J Virol *81*, 718-731.

761   Tacheva-Grigorova, S.K., Santos, A.J., Boucrot, E., and Kirchhausen, T. (2013). Clathrin-

762   mediated endocytosis persists during unperturbed mitosis. Cell Rep *4*, 659-668.

763   Ujike, M., and Taguchi, F. (2015). Incorporation of spike and membrane glycoproteins

764   into coronavirus virions. Viruses *7*, 1700-1725.

765   V'Kovski, P., Kratzel, A., Steiner, S., Stalder, H., and Thiel, V. (2020). Coronavirus biology

766   and replication: implications for SARS-CoV-2. Nat Rev Microbiol.

767   Wang, Y., Grunewald, M., and Perlman, S. (2020). Coronaviruses: An Updated Overview

768   of Their Replication and Pathogenesis. Methods Mol Biol *2203*, 1-29.

769   Whitman, J.D., Hiatt, J., Mowery, C.T., Shy, B.R., Yu, R., Yamamoto, T.N., Rathore, U.,

770   Goldgof, G.M., Whitty, C., Woo, J.M.*, et al.* (2020). Evaluation of SARS-CoV-2 serology

771   assays reveals a range of test performance. Nat Biotechnol *38*, 1174-1183.

772   Wrapp, D., Wang, N., Corbett, K.S., Goldsmith, J.A., Hsieh, C.L., Abiona, O., Graham,

773   B.S., and McLellan, J.S. (2020). Cryo-EM structure of the 2019-nCoV spike in the

774   prefusion conformation. Science *367*, 1260-1263.

775   Yao, H., Song, Y., Chen, Y., Wu, N., Xu, J., Sun, C., Zhang, J., Weng, T., Zhang, Z., Wu,

776   Z.*, et al.* (2020). Molecular Architecture of the SARS-CoV-2 Virus. Cell *183*, 730-738

777   e713.

778   Zhou, P., Yang, X.L., Wang, X.G., Hu, B., Zhang, L., Zhang, W., Si, H.R., Zhu, Y., Li, B.,

779   Huang, C.L.*, et al.* (2020). A pneumonia outbreak associated with a new coronavirus of

780   probable bat origin. Nature *579*, 270-273.

781   Zhou, X., Vink, M., Klaver, B., Berkhout, B., and Das, A.T. (2006). Optimization of the Tet-

782   On system for regulated gene expression through viral evolution. Gene Ther *13*, 1382-
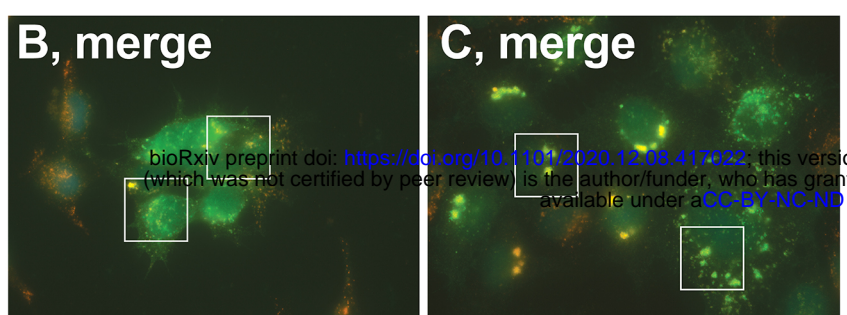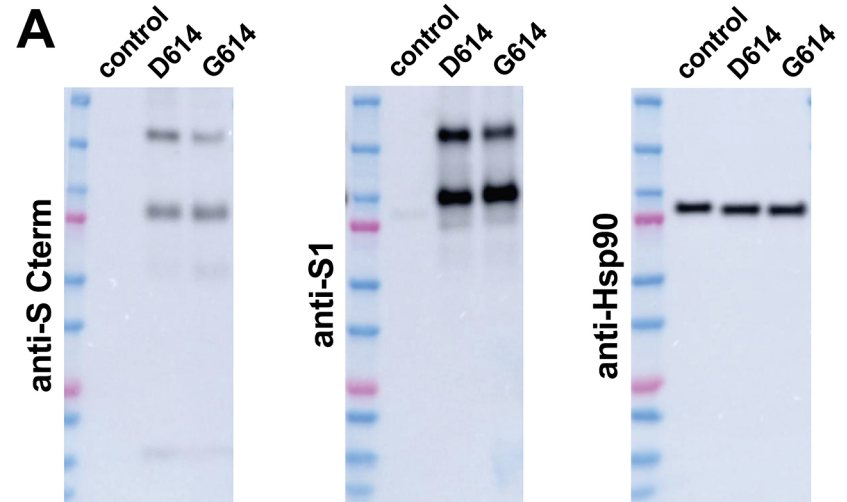
783   1390.

784
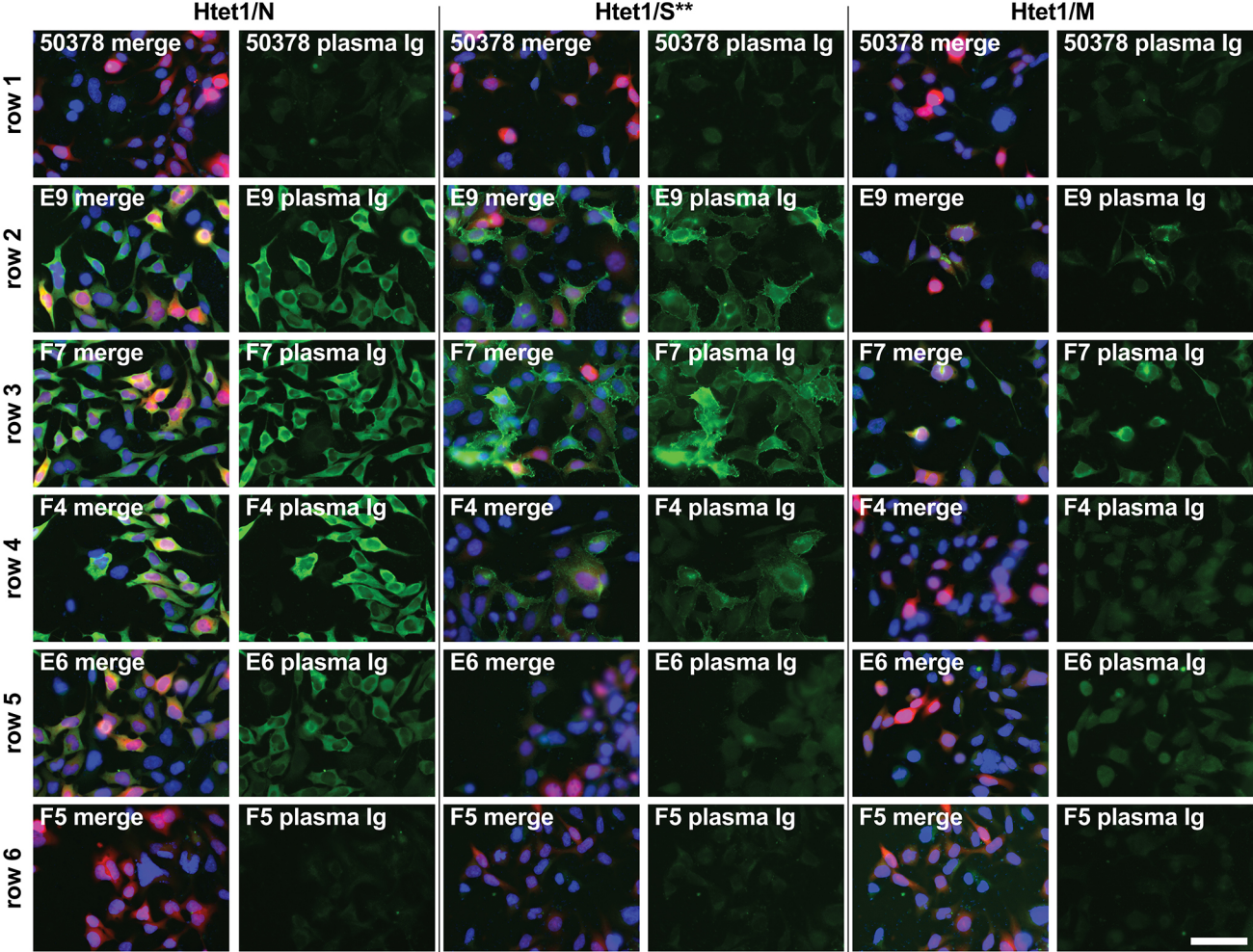
Figure 1
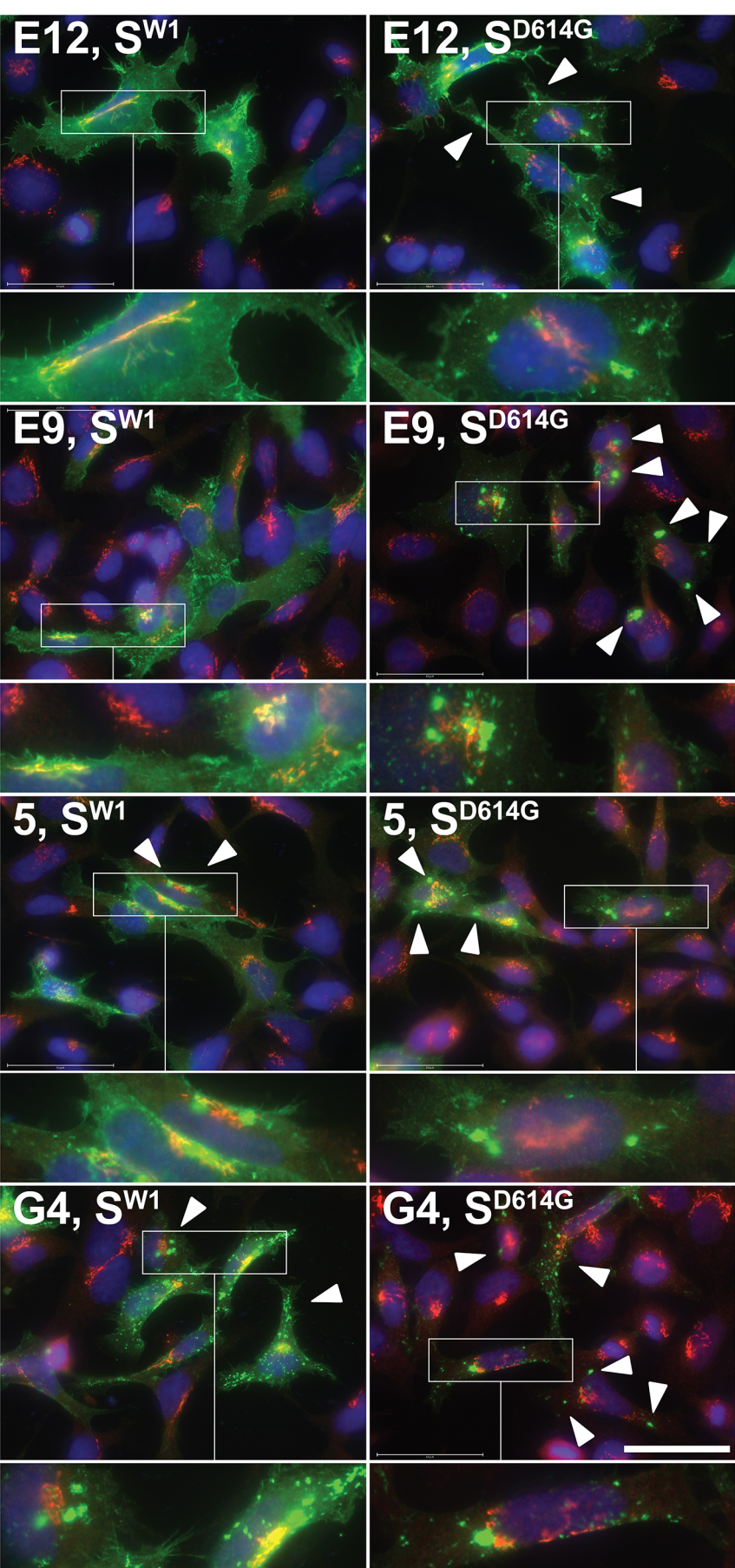
Figure 2
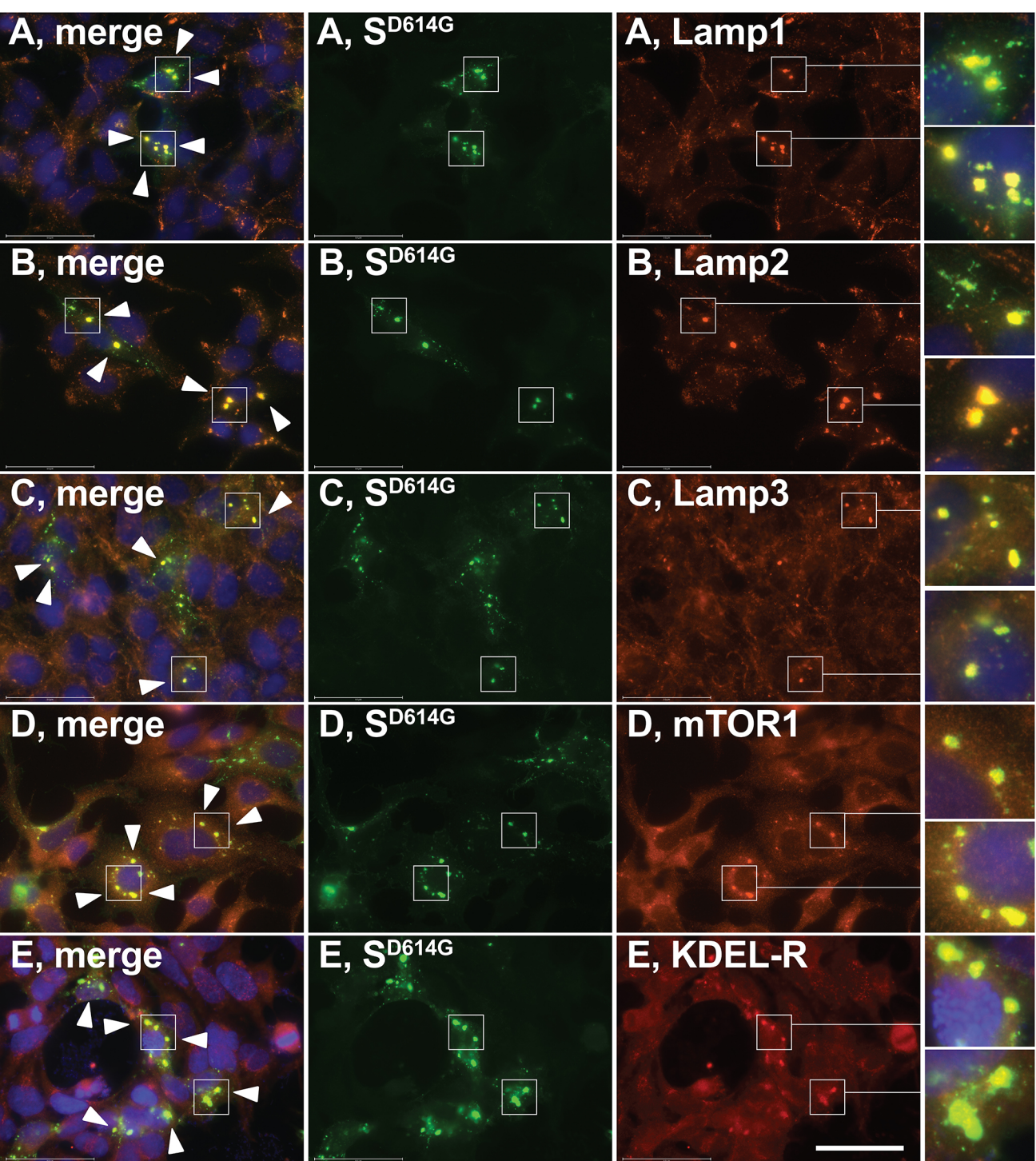
Figure 3
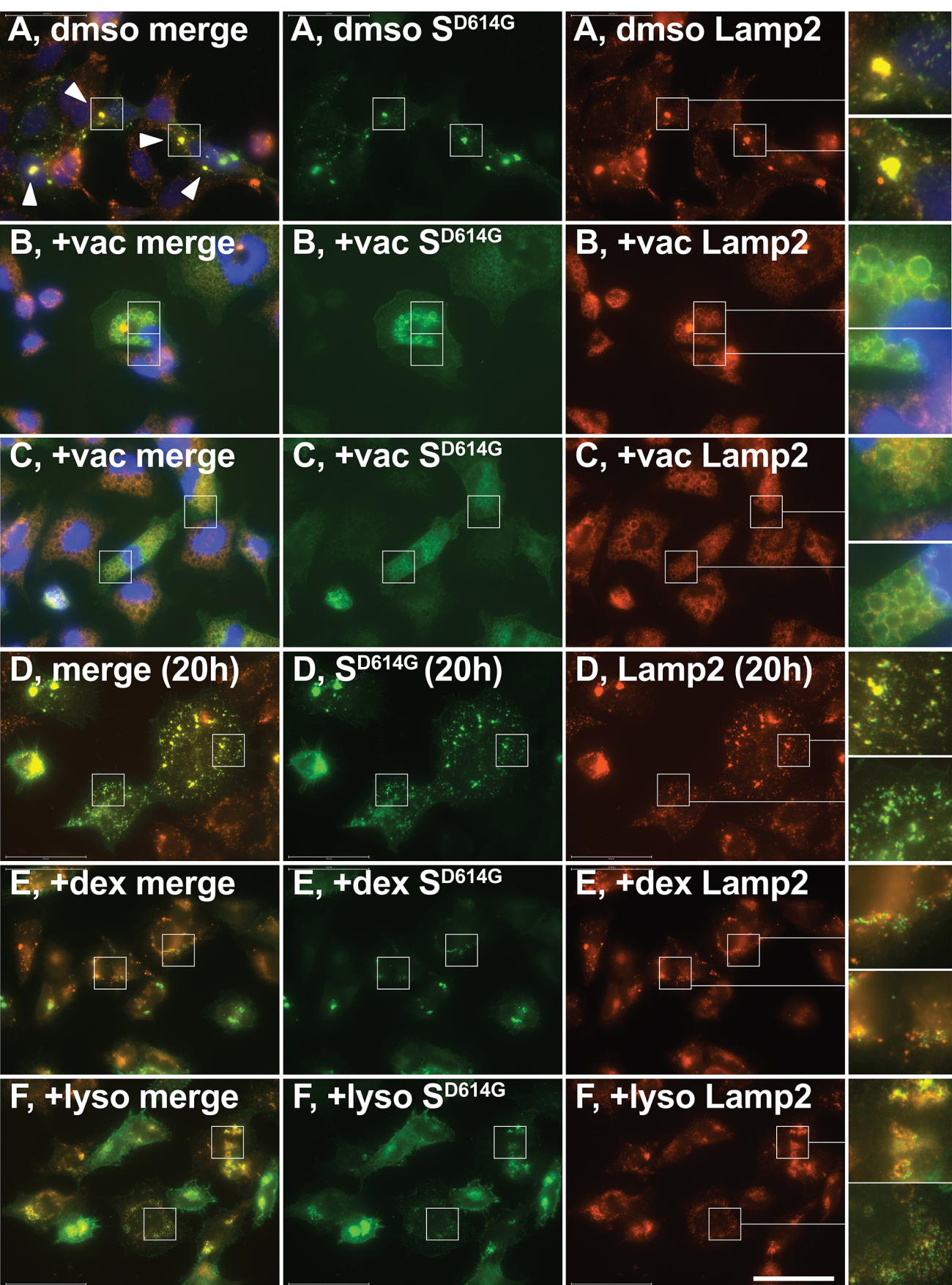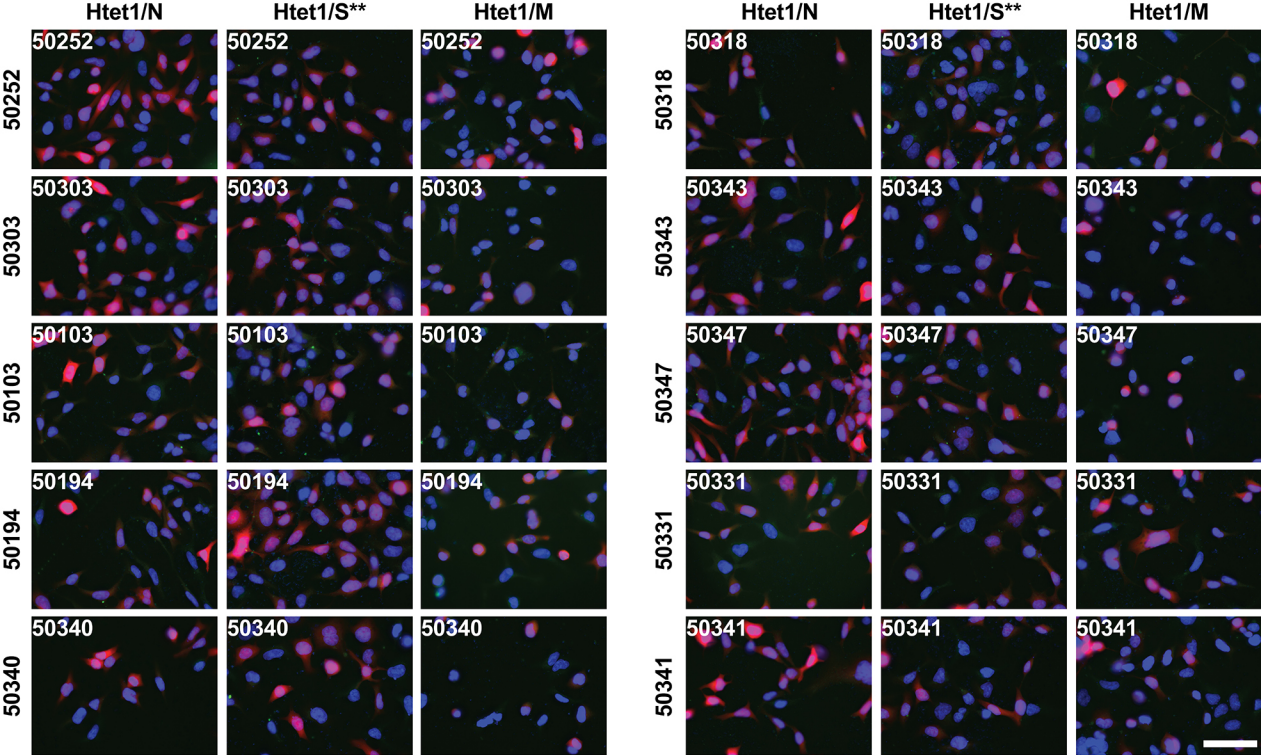
Figure 4
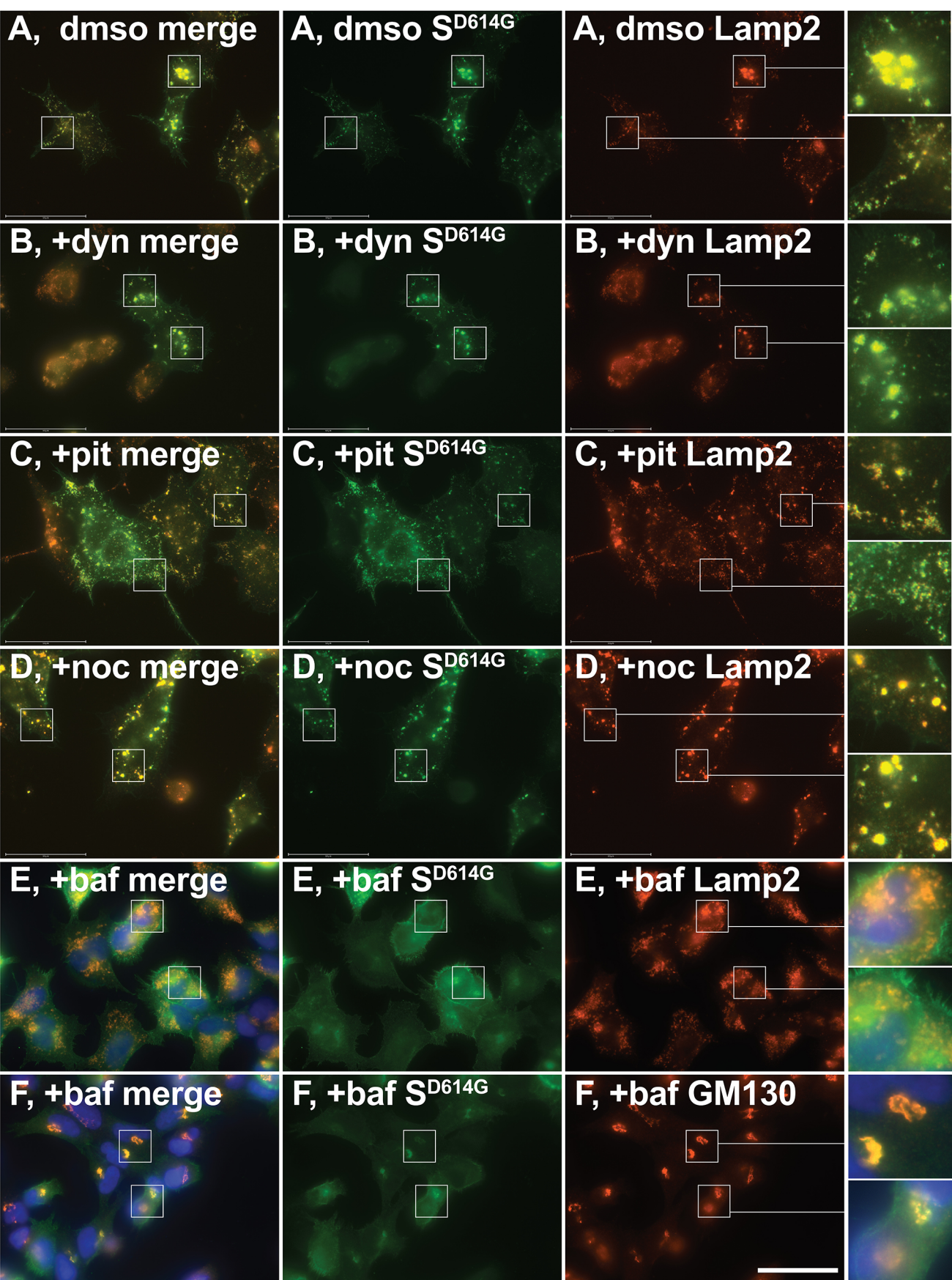
Figure 5
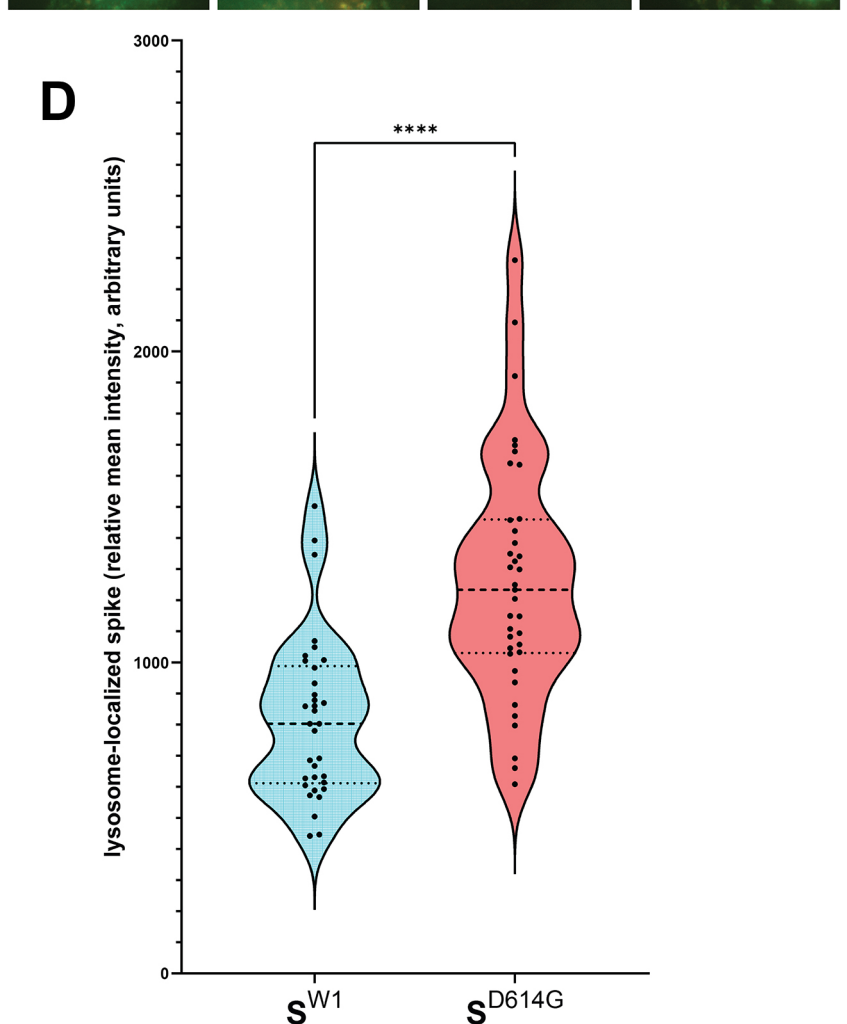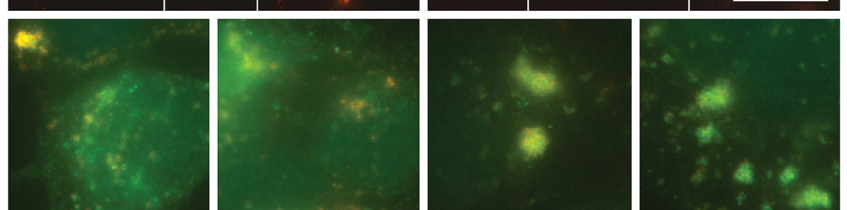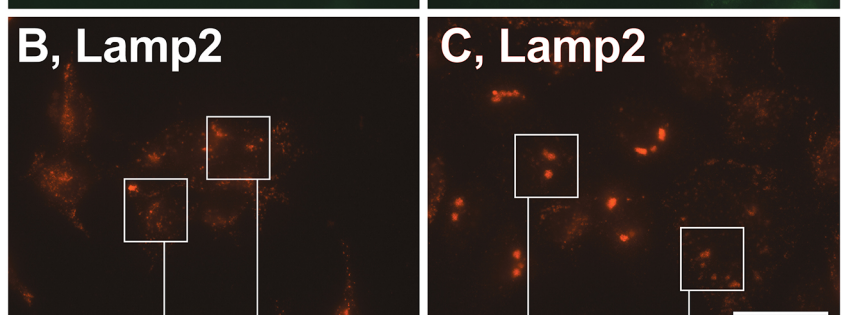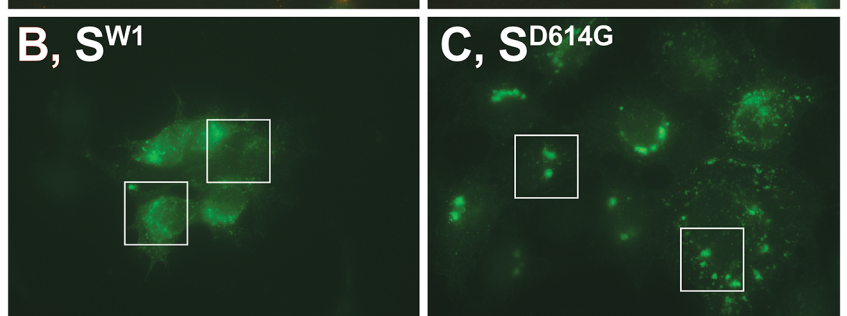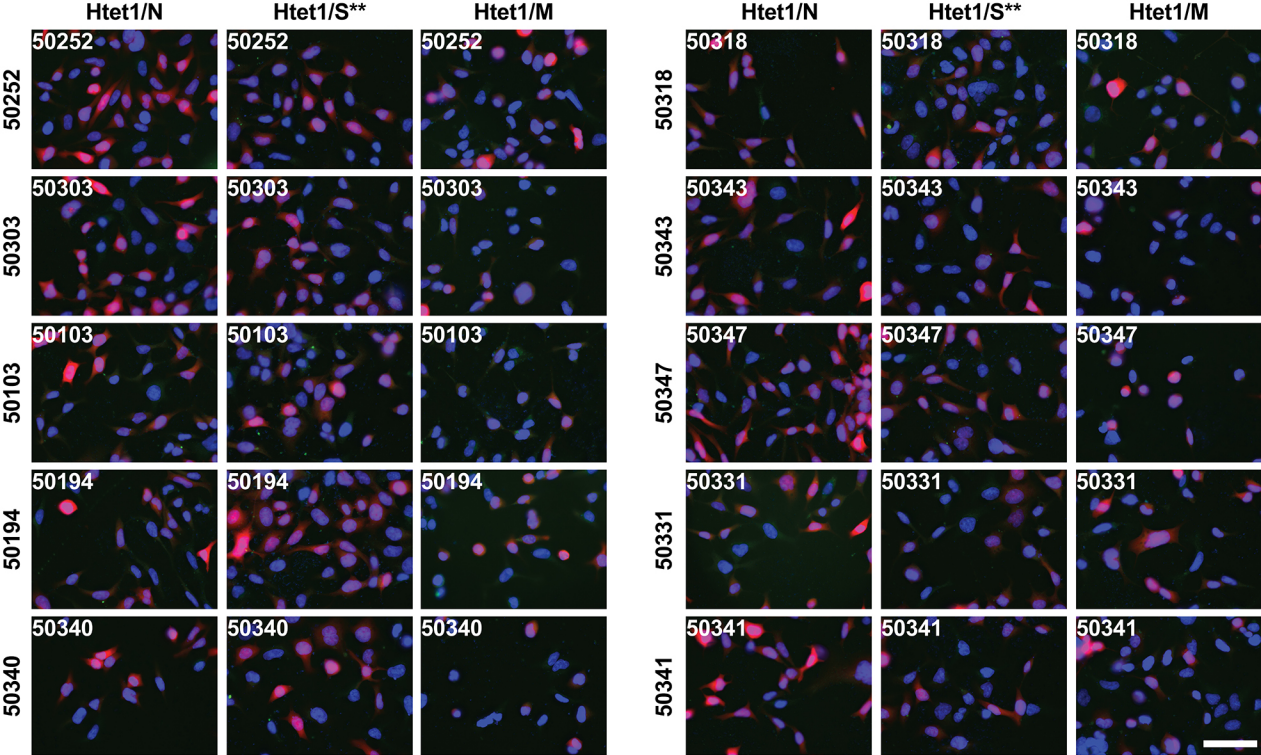
Figure 6
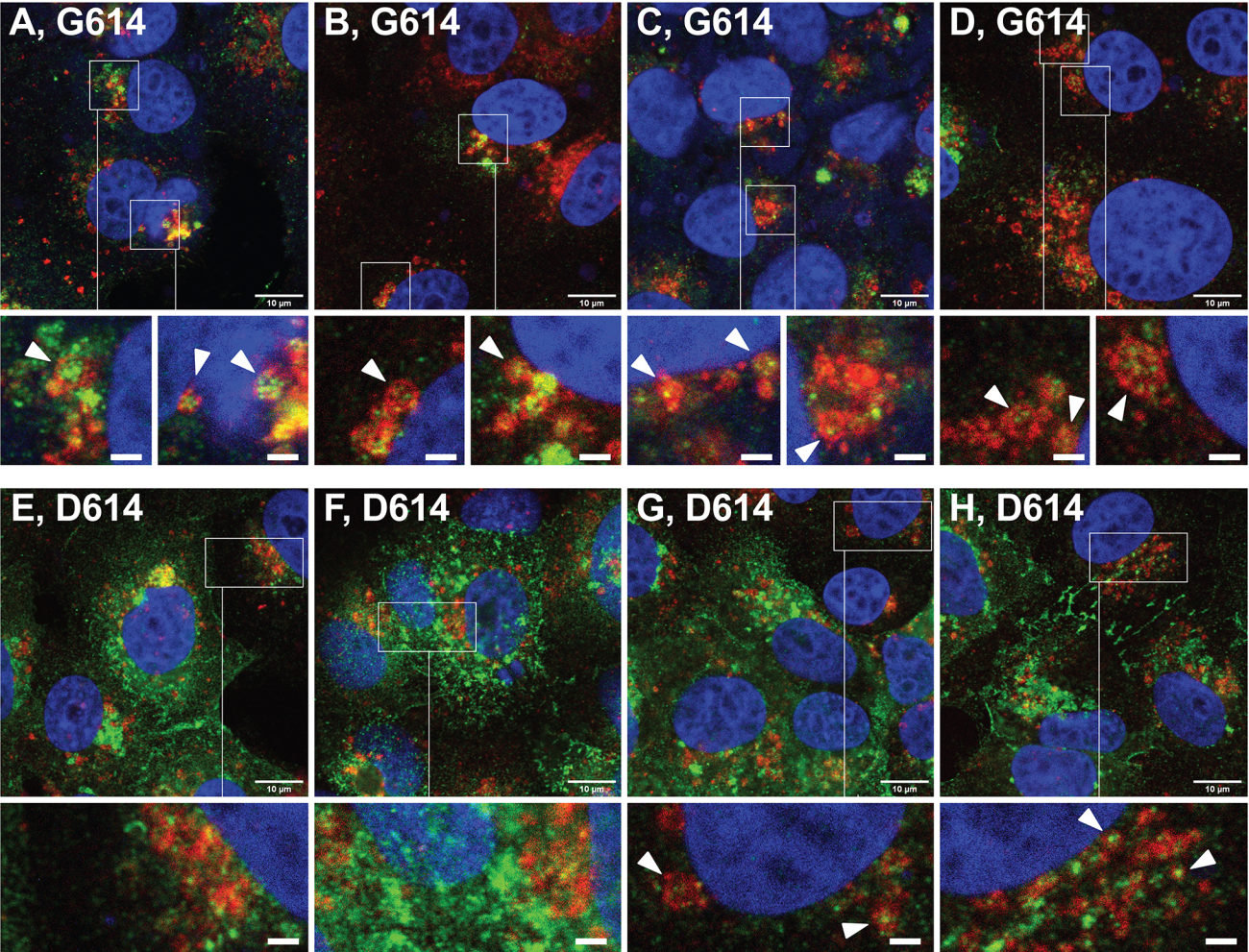
Figure 7
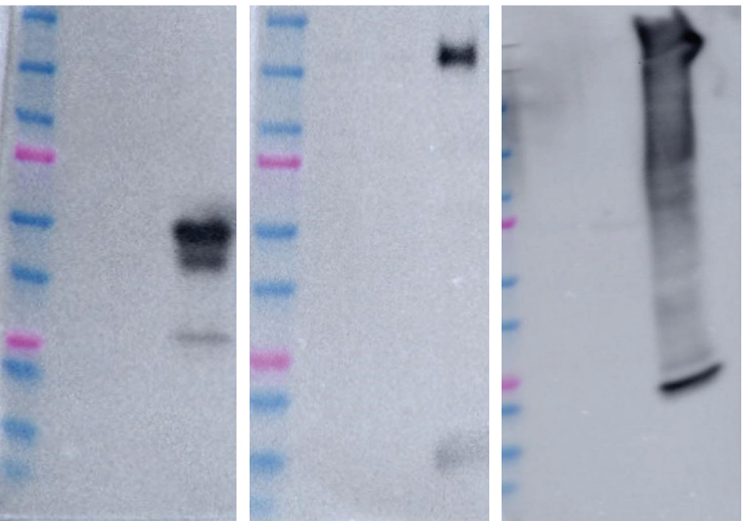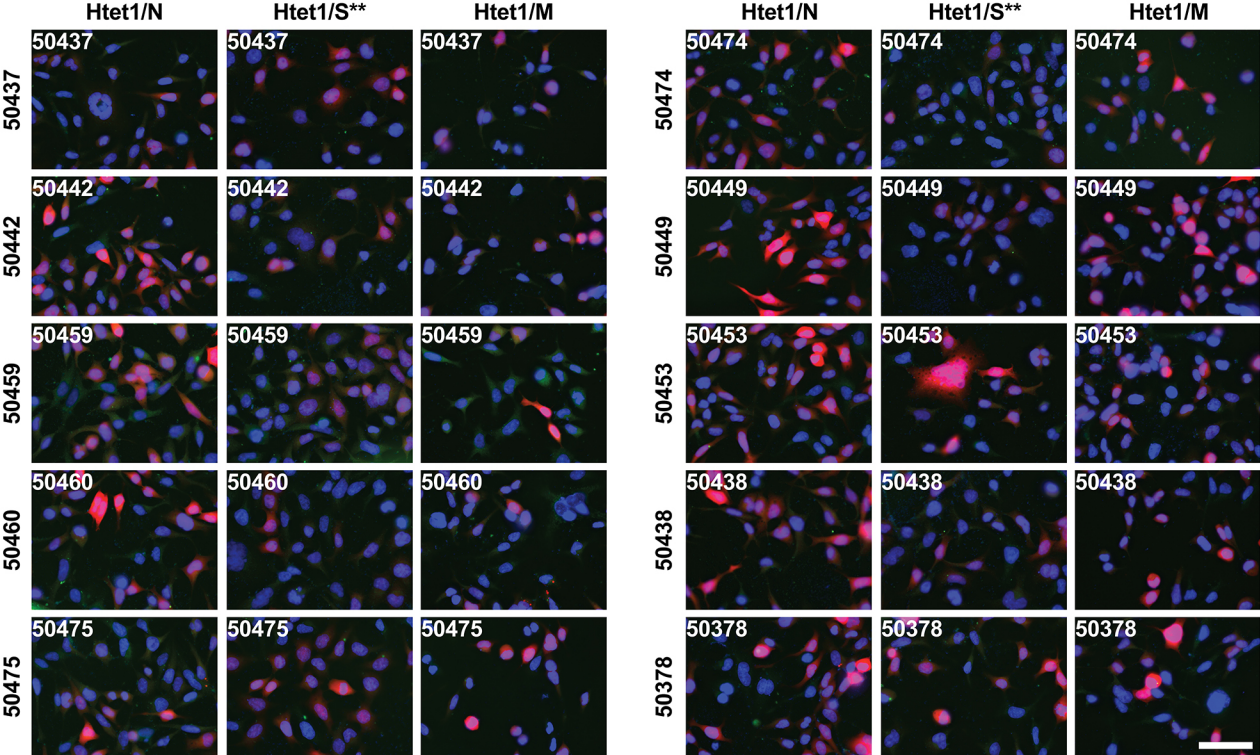
Supplemental figure 1
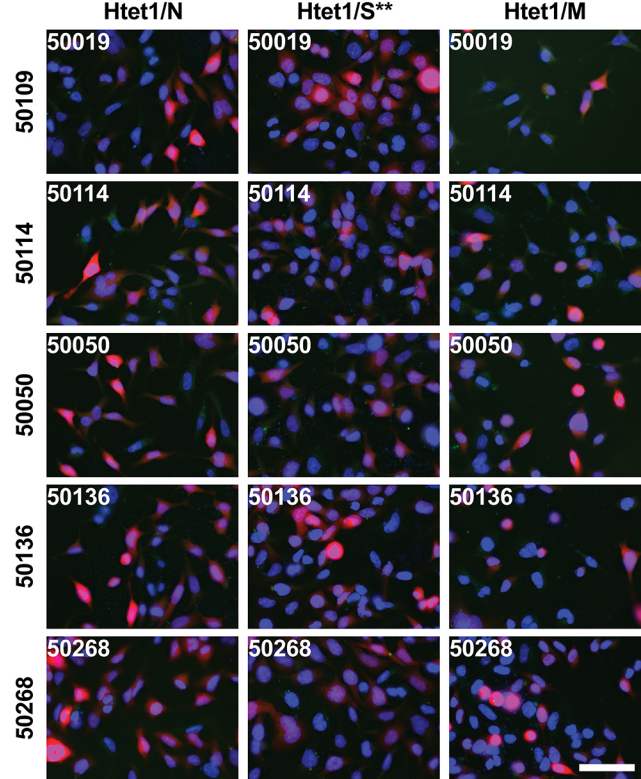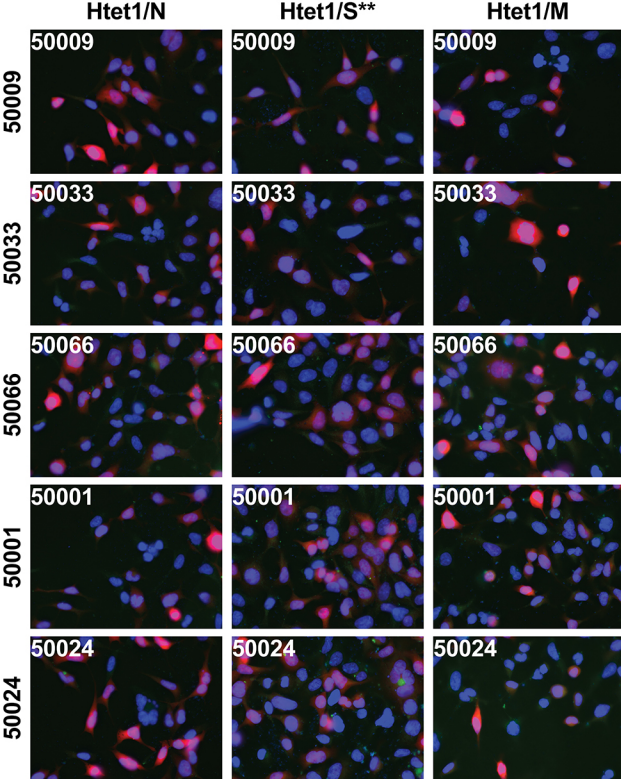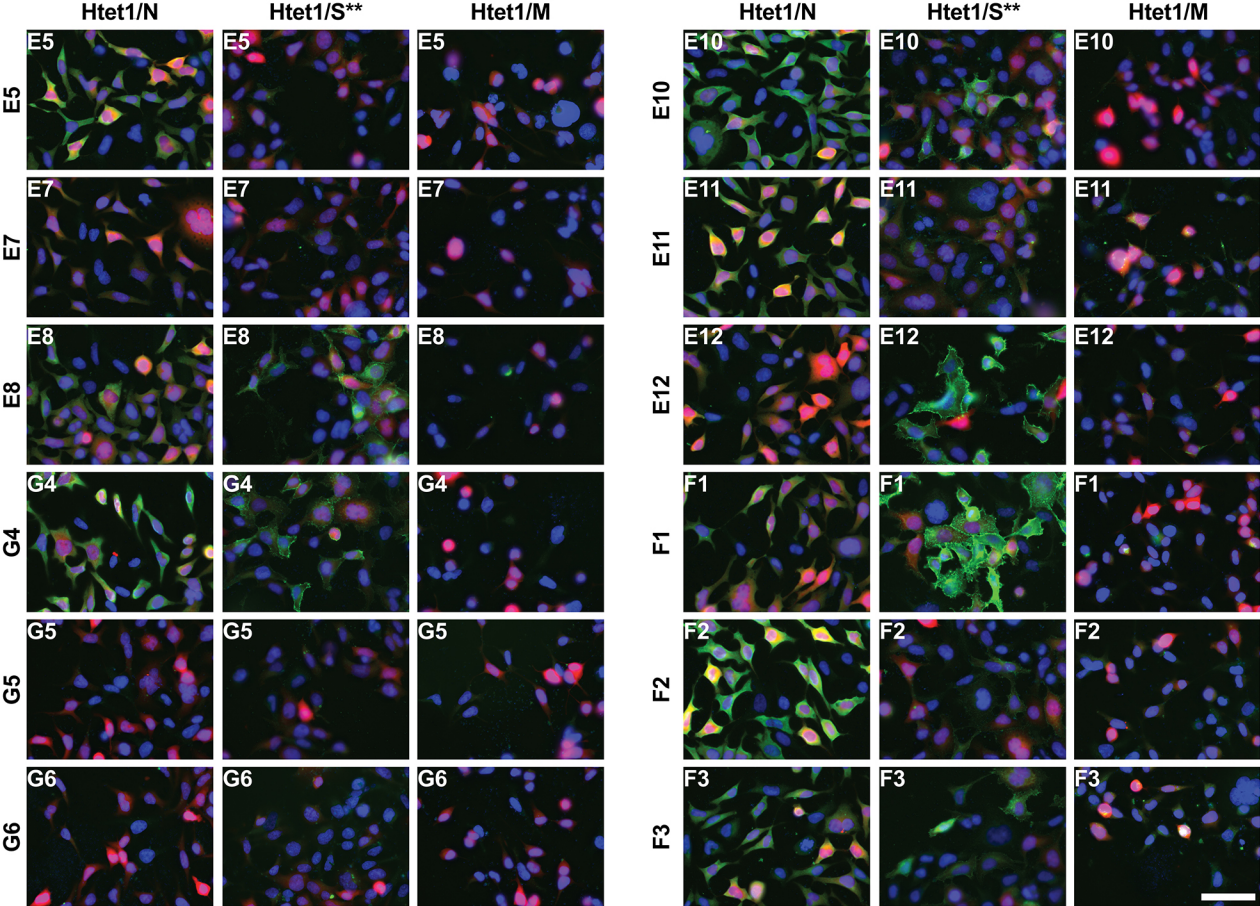
Supplemental figure 2
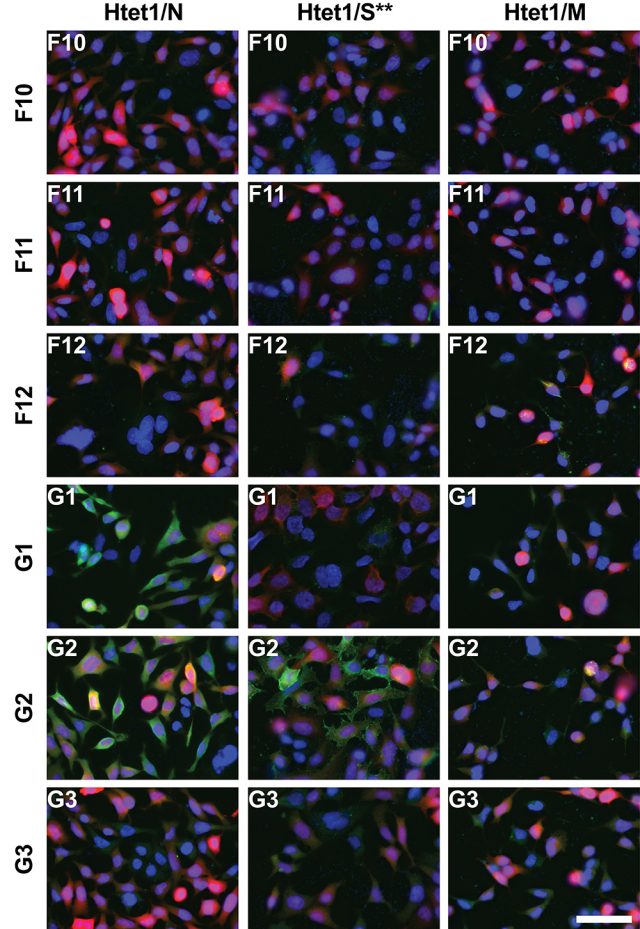
Supplemental figure 3

Supplemental figure 4

Supplemental figure 5

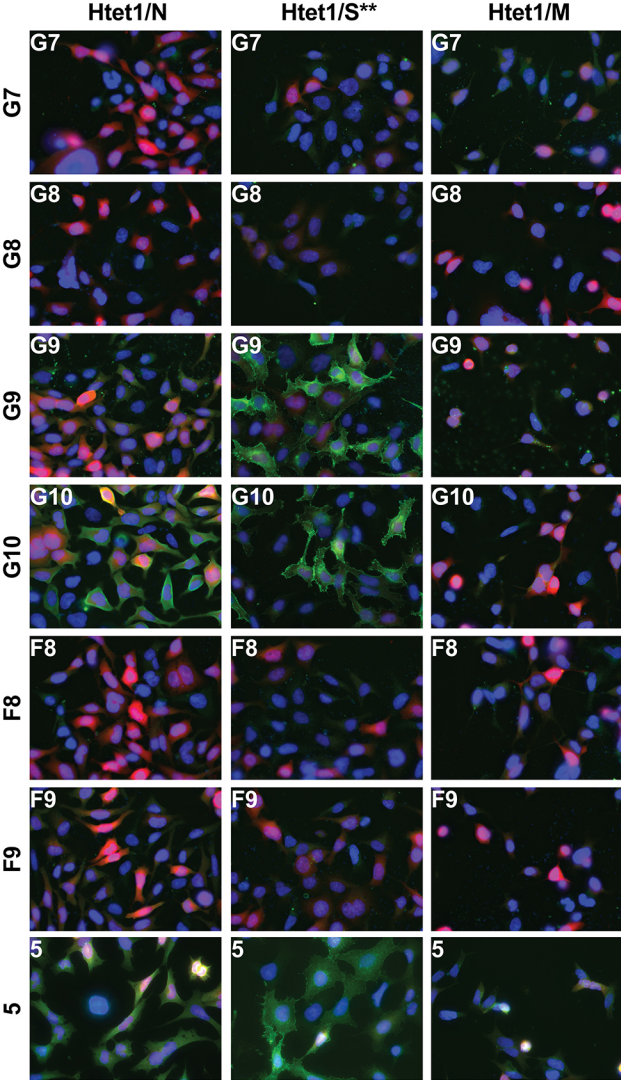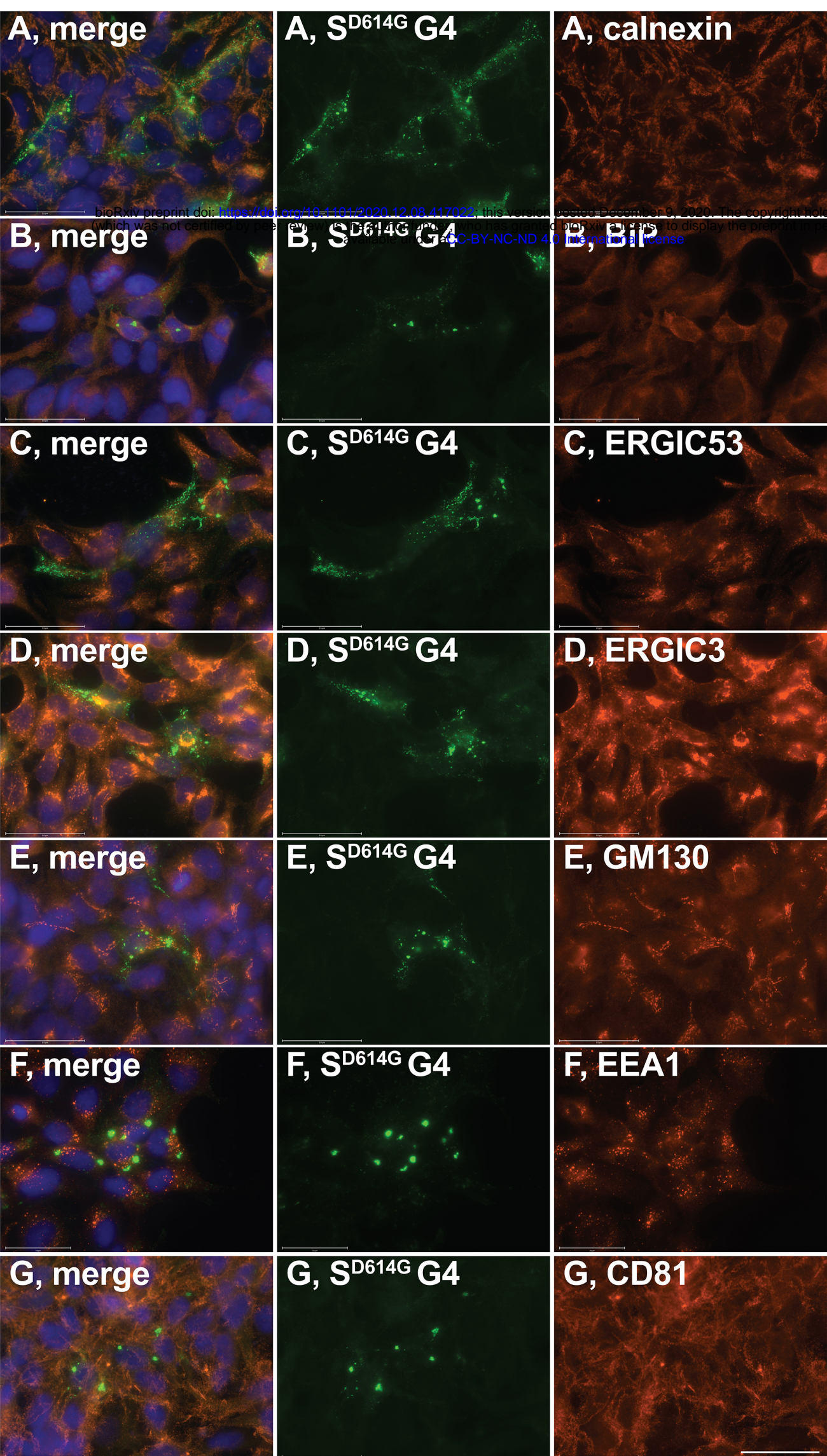**Supplemental figure 6**

Supplemental figure 7

Supplemental figure 8